



Abschlussarbeit im Bachelorstudiengang Physik

# Investigation of the noise performance of silicon drift detectors for the TRISTAN project

Untersuchung des Rauschverhaltens von Siliziumdriftdetektoren für  
das TRISTAN Projekt

Christina Bruch

02. Oktober 2020

Erstgutachter (Themensteller): Prof. Dr. Susanne Mertens  
Zweitgutachter: Prof. Dr. Björn Gabrecht

# Contents

<b>Abstract</b> . . . . .	ix
<b>1 Neutrinos, the KATRIN experiment and the TRISTAN project</b> . . . . .	1
1.1 Neutrino physics . . . . .	1
1.1.1 Neutrinos in the Standard Model . . . . .	1
1.1.2 Neutrino oscillations and neutrino mixing . . . . .	1
1.1.3 Neutrinos beyond the Standard Model . . . . .	3
1.2 The KATRIN experiment . . . . .	3
1.2.1 Measurement principle . . . . .	4
1.2.2 Experimental setup . . . . .	5
1.3 The TRISTAN project . . . . .	6
1.3.1 Signature of a sterile neutrino on the beta decay spectrum . . . . .	6
1.3.2 Detector requirements . . . . .	7
<b>2 TRISTAN prototype detector setup</b> . . . . .	9
2.1 Working principle of a Silicon Drift Detector . . . . .	9
2.2 Experimental setup . . . . .	10
2.2.1 Test stand . . . . .	10
2.2.2 TRISTAN detector prototypes . . . . .	12
2.2.3 $^{55}\text{Fe}$ source . . . . .	14
2.3 Noise components . . . . .	15
2.3.1 Fano limit . . . . .	15
2.3.2 Electronic noise sources . . . . .	16
2.3.3 Noise in a charge sensitive pre-amplifier . . . . .	16
<b>3 Noise density measurements</b> . . . . .	19
3.1 Waveform preparation . . . . .	19
3.2 Noise density spectrum of the S0-7-1 detector . . . . .	20
3.3 Noise density of different detectors . . . . .	22
3.3.1 Comparison of different generations of detectors . . . . .	22
3.3.2 Comparison of different detectors of same generation . . . . .	24
3.4 Temperature dependence of the noise density spectrum . . . . .	25

<b>4 Noise curve measurements and simulations . . . . .</b>	<b>29</b>
4.1 Energy resolution of the S0-7-1 detector . . . . .	29
4.2 Verification of measurements with waveform simulation . . . . .	31
4.3 Determination of the noise coefficients of the trapezoidal filter . . . . .	33
4.4 Analysis of the influence of the gap time of a trapezoidal filter . . . . .	37
4.5 Analysis of the influence of the peaking time on the peak position . . . . .	38
<b>5 Conclusion . . . . .</b>	<b>41</b>
<b>Bibliography . . . . .</b>	<b>43</b>

# List of Figures

1.1	Standard Model of particle physics for fermions . . . . .	2
1.2	Tritium spectrum with zoom on end point . . . . .	4
1.3	Experimental setup of KATRIN experiment . . . . .	5
1.4	Signature of sterile neutrino in tritium spectrum . . . . .	7
1.5	Scheme of final TRISTAN detector . . . . .	8
2.1	Structure of a Silicon Drift Detector . . . . .	10
2.2	Picture of detector board inside the vacuum chamber . . . . .	11
2.3	Picture of the test stand . . . . .	11
2.4	Working principle of a trapezoidal filter . . . . .	12
2.5	Scheme of pixel arrangement of 7-pixel detectors . . . . .	13
2.6	Picture of the electronic side of the S0-7-2 detector . . . . .	14
2.7	Exemplary $^{55}\text{Fe}$ spectrum with fit . . . . .	15
3.1	Exemplary waveform of the S0-7-2 detector . . . . .	20
3.2	Fit to the noise density of the S0-7-1 detector . . . . .	21
3.3	Comparison of noise density of all pixels of the S0-7-1 detector . . . . .	23
3.4	Comparison of the noise density of the S0-1 and S0-7-1 detector . . . . .	24
3.5	Comparison of the noise density of the S0-7-1 and S0-7-2 detector . . . . .	25
3.6	Temperature dependence of the noise density of the S0-7-2 detector . . . . .	26
3.7	Temperature dependence of the leakage current of the S0-7-2 detector . . . . .	27
3.8	Comparison of the leakage current of the S0-1 and S0-7-2 detector . . . . .	27
4.1	Noise curve of the S0-7-1 detector . . . . .	30
4.2	Comparison of noise curves of S0-7-1 and S0-1 detector . . . . .	31
4.3	Comparison of simulated and measured noise density . . . . .	32
4.4	Comparison of simulated and measured noise curve . . . . .	34
4.5	Comparison of measured and expected noise curve . . . . .	36
4.6	Influence of the gap time on the energy resolution . . . . .	37
4.7	Influence of the peaking time on the peak position . . . . .	39



# List of Tables

2.1 X-ray energies of $^{55}\text{Fe}$ for the measurements . . . . .	14
2.2 Calculated noise coefficients . . . . .	18
3.1 Physical values extracted from the fit of the noise density . . . . .	22
4.1 Comparison of calculated and fitted noise coefficients . . . . .	35
4.2 Comparison of physical values extracted from the noise density and the noise curve . . . . .	35
4.3 Expected physical values for the S0-7-1 detector . . . . .	36



# Abstract

Sterile neutrinos are a minimal extension of the Standard Model of particles. If they exist, they would present answers to numerous open questions in astroparticle physics and cosmology. A sterile neutrino with a mass in the keV regime would be a dark matter candidate.

Investigating beta decay spectra is a promising way to search for sterile neutrinos, as the mass eigenstate of a sterile neutrino would manifest itself as a kink-like distortion of the spectrum. Therefore, the TRISTAN project will take advantage of the setup of the KATRIN experiment while providing a new detector system suited for high-rate  $\beta$ -spectroscopy in order to detect the signature of a sterile neutrino.

For the imprints of the sterile neutrino on the spectrum to be visible, a large number of  $\beta$ -electrons must be detected and the energy of the incoming  $\beta$ -electrons has to be known precisely. For this task, silicon drift detectors are suitable. By minimizing the electronic noise in the signal, they are specially optimized to provide an excellent energy resolution for high signal rates.

In this work, the noise behaviour of the current TRISTAN detector prototype was investigated and compared to a detector of the previous generation as well as one of the same generation. For this purpose, x-rays from an  $^{55}\text{Fe}$ -source have been measured. The analysis of the noise has been performed in the frequency domain as well as in the time domain.

A major focus of this thesis was the modelling of the noise spectrum. The model is based on a theoretical relationship of key detector parameters such as capacitance, transconductance and leakage current with the noise level. It allows to extract information about the detector by fitting the model to the data. For the new detector however, the results of the noise analysis indicate an additional noise component in the data, which is not described by the model. An elevated noise level in the frequency range of  $2 \cdot 10^5 - 1 \cdot 10^7$  Hz was found. Compared to the old detector, the noise level is increased by about a factor 5 in this region. As a consequence, the energy resolution at room temperature at 6 keV for a peaking time of  $1 \mu\text{s}$  is  $\Delta E_{\text{FWHM}} = 230 \text{ eV}$ , while for the old detector  $\Delta E_{\text{FWHM}} = 166 \text{ eV}$  was found. This is still acceptable for the TRISTAN project. However, the source of this noise needs to be investigated.

Moreover, the dependence of the noise on temperature was considered. As expected, a decrease of noise at low frequencies was found due to a reduced leakage current.

However, the noise in the above-mentioned frequency range is almost independent of temperature.

In the field of noise characterisation, the so-called noise curve is often used to characterise the detector. Here the noise level is displayed as a function of the peaking time of the pulse shaper. In order to simulate a noise curve, a large sample of individual waveforms with the noise level obtained from the noise density fit were generated. The energy resolution was then extracted by applying a trapezoidal filter of varying peaking times. A good agreement with the shape of data was found with a small offset at cool temperatures.

Through this procedure, the correct noise coefficients of the trapezoidal filter were derived, which allowed to extract the relevant detector information directly from the measured noise curve.

# Chapter 1

## Neutrinos, the KATRIN experiment and the TRISTAN project

### 1.1 Neutrino physics

In this section, a short overview of neutrino physics will be given, starting with an introduction of the neutrino as a Standard Model particle in subsection 1.1.1. Subsection 1.1.2 explains neutrino mixing, which is not covered in the Standard Model and leads to neutrino theories beyond the Standard Model, including right-handed sterile neutrinos in subsection 1.1.3.

#### 1.1.1 Neutrinos in the Standard Model

The neutrino is part of the Standard Model of particle physics (SM), which describes the fundamental particles and interactions. The SM consists of six quarks of different flavours with charges of  $q = -\frac{1}{3}$  or  $q = +\frac{2}{3}$ , that can be both of left-handed or right-handed chirality. It also includes the three known charged leptons, the electron, the myon and the tau lepton with a charge of  $q = -1$  as well as their anti-leptons. To each charged lepton flavour there is a corresponding neutral lepton, the neutrino (or anti-neutrino in case of anti-leptons). But in contrast to quarks and charged leptons, it was proven in the Goldhaber experiment, that neutrinos only come left-handed, while anti neutrinos are always right-handed [1]. Figure 1.1 shows the SM. The neutrino is expected to have neither mass nor electric or colour charge in the SM. It can only interact via weak interaction, making neutrinos unique in the SM and difficult to detect.

#### 1.1.2 Neutrino oscillations and neutrino mixing

However, with the discovery of neutrino oscillations by the SNO experiment, it became clear that the nature of neutrinos is not described accurately in the SM [3]. Neutrinos can change their flavour between the point of origin and the point of

Three Generations  
of Matter (Fermions) spin ½

	I	II	III
mass →	2.4 MeV	1.27 GeV	171.2 GeV
charge →	$\frac{2}{3}$	$\frac{2}{3}$	$\frac{2}{3}$
name →	<b>u</b> up	<b>c</b> charm	<b>t</b> top
	Left Right	Left Right	Left Right
Quarks	4.8 MeV	104 MeV	4.2 GeV
	$-\frac{1}{3}$	$-\frac{1}{3}$	$-\frac{1}{3}$
	<b>d</b> down	<b>s</b> strange	<b>b</b> bottom
	Left Right	Left Right	Left Right
Leptons	0 eV	0 eV	0 eV
	$0$	$0$	$0$
	<b><math>\nu_e</math></b> electron neutrino	<b><math>\nu_\mu</math></b> muon neutrino	<b><math>\nu_\tau</math></b> tau neutrino
	Left	Left	Left
	0.511 MeV	105.7 MeV	1.777 GeV
	-1	-1	-1
	<b>e</b> electron	<b><math>\mu</math></b> muon	<b><math>\tau</math></b> tau
	Left Right	Left Right	Left Right

Figure 1.1: The Standard Model of particle physics (SM) with six quarks of different charges and flavors, three flavors of charged leptons as well as the corresponding neutral leptons, the neutrino. Note that quarks and charged leptons come in left- and right-handed chirality, while neutrinos are always left-handed. Adapted from [2].

interaction due to the mixing of flavour and mass eigenstates of neutrinos. It is described by the **P**ontecorvo-**M**aki-**N**akagawa-**S**akata (PMNS) matrix, shown in equation (1.1).

$$\underbrace{\begin{pmatrix} \nu_e \\ \nu_\mu \\ \nu_\tau \end{pmatrix}}_{\text{flavour eigenstates}} = \underbrace{\begin{pmatrix} U_{e1} & U_{e2} & U_{e3} \\ U_{\mu1} & U_{\mu2} & U_{\mu3} \\ U_{\tau1} & U_{\tau2} & U_{\tau3} \end{pmatrix}}_{\text{PMNS matrix}} \underbrace{\begin{pmatrix} \nu_1 \\ \nu_2 \\ \nu_3 \end{pmatrix}}_{\text{mass eigenstates}} \quad (1.1)$$

Instead of each flavour corresponding to one mass, as it is the case with charged leptons, each neutrino flavour is a coherent superposition of the three mass eigenstates  $\nu_1$ ,  $\nu_2$ ,  $\nu_3$  with masses  $m_1$ ,  $m_2$ ,  $m_3$ . These mass eigenstates propagate differently, leading to neutrino oscillations. Consequently, they are only possible if neutrinos have a non-zero mass.

While the oscillation probability is proportional to the mass difference  $\Delta m^2$  of the

neutrinos involved, it does not depend the sign of  $\Delta m^2$  and give no quantitative information about the absolute masses  $m_1$ ,  $m_2$ ,  $m_3$  [4]. One experiment investigating the effective electron anti-neutrino mass is the **K**arlsruhe **T**ritium **N**eutrino **E**xperiment (KATRIN), which will be addressed in section 1.2.

### 1.1.3 Neutrinos beyond the Standard Model

A natural extension of the Standard Model is the introduction of a right-handed neutrino. This would increase the uniformity of the Standard Model as well as provide an explanation for the neutrino mass, since only particles with both left-handed and right-handed chirality can have a Dirac mass. As neutrinos only interact weakly, right-handed neutrinos would not interact directly at all, making them sterile neutrinos in contrast to their left-handed counterparts, the active neutrino. However, sterile neutrinos would be detectable due to the mixing of the mass eigenstates of sterile and active neutrinos [5].

Sterile neutrinos could also explain the small effective neutrino mass. The experimental limit for the neutrino mass is currently assumed to be under 1.1 eV (90 % CL) [6], while physically motivated neutrino mass models predict an upper limit of the sum of neutrino masses of  $\sum m_\nu \lesssim 0.26$  eV (95 % CI) [7]. If neutrinos are Majorana particles, meaning they can transition from a neutrino to an anti-neutrino, a heavy sterile neutrino would lead to a light active neutrino due to the See-Saw mechanism [8].

In addition, sterile neutrinos with a mass  $\mathcal{O}(\text{keV})$  are candidates for warm and cold dark matter [5]. Although the mass of sterile neutrinos can be anywhere from  $\mathcal{O}(\text{eV})$  to  $\mathcal{O}(\text{TeV})$ , this thesis will focus on the search for keV-sterile neutrinos with the TRISTAN project described in section 1.3.

## 1.2 The KATRIN experiment

To investigate the effective neutrino mass and improve the upper limit, the **K**arlsruhe **T**ritium **N**eutrino (KATRIN) experiment measures the tritium beta decay spectrum. Relying only on kinematic relations and energy-momentum conservation, it is largely model-independent. Within three years of data taking, KATRIN is expected to set the upper limit for a neutrino mass to  $0.2 \frac{\text{eV}}{c^2}$  with a 90 % confidence level if no positive signal is observed. If a neutrino mass signal is found, it will have a discovery potential of  $5\sigma$  ( $3\sigma$ ) for  $m_\nu = 0.35 \frac{\text{eV}}{c^2}$  ( $m_\nu = 0.3 \frac{\text{eV}}{c^2}$ ) [9]. In subsection 1.2.1, the imprint of the neutrino on the tritium beta decay will be discussed, before giving a quick overview of the experimental setup of the KATRIN experiment in subsection 1.2.2

### 1.2.1 Measurement principle

Tritium decays via beta decay in a helium atom along with an electron and an anti-electron neutrino:



Assuming a neutrino with mass zero, the endpoint energy of this decay is determined by the mass difference of the tritium and helium, amounting to  $E_0 \approx 18.6 \text{ keV}$ . A non-zero neutrino mass alters the tritium beta decay especially in its endpoint region, as the maximal energy carried by the beta electron never reaches the endpoint energy  $E_0$  due to energy conservation. Instead, a fraction of the decay energy has to be expended for the creation of the electron anti-neutrino, resulting in a maximal beta electron energy of

$$E_{e, \text{max}} = E_0 - m_\nu c^2. \quad (1.3)$$

The impact of a non-zero neutrino mass on the tritium beta decay spectrum is shown in figure 1.2. The neutrino mass is determined by fitting the tritium spectrum close to the endpoint.

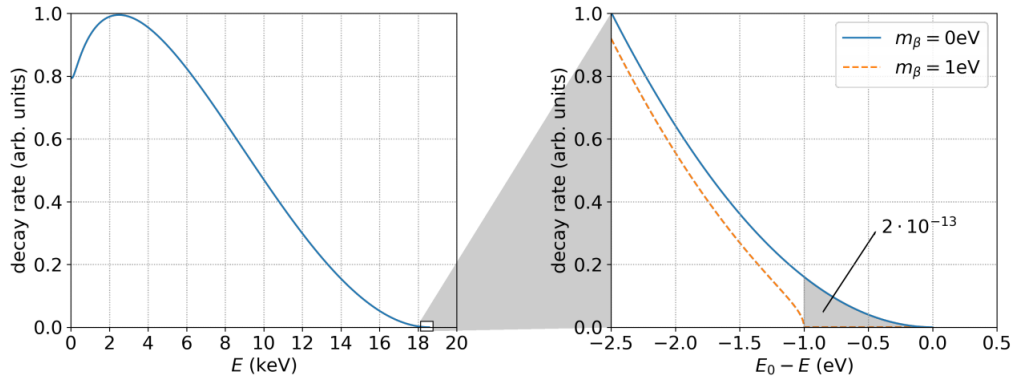


Figure 1.2: Tritium spectrum with zoom on end point. On the left, the full tritium spectrum is shown. The endpoint energy amounts to  $E_0 = 18.6 \text{ keV}$ . On the right, the spectrum is zoomed in on the endpoint. If the neutrino was massless as in the Standard Model, the endpoint will be reached. This is represented by the blue line. For a non-zero neutrino mass, in this case  $m_\nu = 1 \text{ eV}$ , illustrated by the dashed orange line, the endpoint energy of the spectrum is less than  $E_0$ . Note that only  $2 \cdot 10^{-11} \%$  of events fall in the shaded area. Adapted from [10].

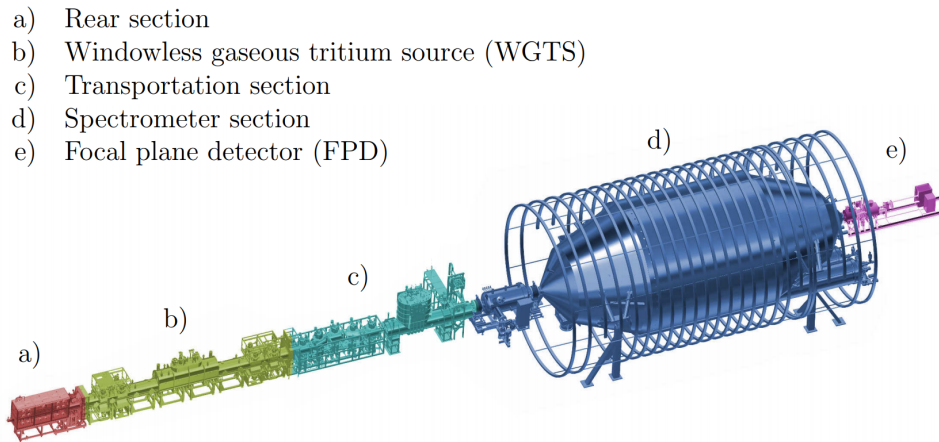


Figure 1.3: Experimental setup of the KATRIN experiment. Adapted from [11].

### 1.2.2 Experimental setup

A scheme of the experimental setup of KATRIN is shown in figure 1.3. In this work however, only the main components are briefly introduced. For a more detailed explanation of the different parts, see [9].

**Windowless Gaseous Tritium Source (WGTS):** The KATRIN experiment uses tritium as a source for beta decay electrons. Tritium has a half life of 12.3 years [12]. In addition, its low endpoint energy results in a relative high rate close to the endpoint compared to sources with higher endpoint energies, therefore minimizing the amount of tritium needed for the measurement. This makes tritium a suitable source for the experiment.

The tritium source is gaseous in order to avoid self-charge effects that would result in a distortion of the spectrum. To avoid scattering and a dead layer for the emitted beta electrons, the source has to be windowless. A crucial point to minimize uncertainties is keeping the tritium source column density of  $5 \cdot 10^{17} \text{ cm}^{-2}$  as stable as possible, aiming for a stability of 0.1% [9]. This is achieved through closed tritium loops and a controlled injection system.

**Spectrometer:** To measure the beta spectrum close to the endpoint, the KATRIN experiment uses an integral measurement, meaning that only electrons with a certain, variable energy pass the spectrometer and reach the detector. This is achieved by a MAC-E-Filter (**M**agnetic **A**diabatic **C**ollimation combined with an **E**lectrostatic **F**ilter). Two superconducting magnets create a magnetic field, which is strong at the

ends of the spectrometer and significantly weaker in the middle. The electrons are guided adiabatically through the spectrometer, where they face a retarding potential in the middle, so that only the electrons with sufficient energy can pass. They are then re-accelerated and collimated onto the detector. The resolution of the spectrometer is determined by the ratio of the magnetic field in the middle of the spectrometer and the magnetic field at the edges [9].

**Focal plane detector:** The detector of the KATRIN experiment consists of a monolithic 148-pixel p-i-n-diode array with an energy resolution of  $\Delta E_{\text{Det}} < 600$  eV [9], [13]. The spectrometer filters out electrons with lower energies and therefore determined the minimal energy of the electrons that passed to the detector. Therefore, the detector itself only counts the incoming electrons, resulting in low count rates.

## 1.3 The TRISTAN project

After KATRIN has completed data taking for the investigation of the effective electron anti-neutrino mass, it is used for the search for sterile neutrinos. Despite sterile neutrinos being non-interacting particles, a kink-like signature would be visible due to the mixing of sterile and active neutrinos. The effective neutrino mass is determined in the endpoint region of the tritium spectrum, where the count rate is low. The sterile neutrino mass, however, could be anywhere from  $\mathcal{O}(\text{eV})$  to  $\gg \mathcal{O}(\text{TeV})$ , leading to new requirements for the detector system. For this reason, the TRISTAN project (**T**ritium **I**nvestigation on **S**terile to **A**ctive **N**eutrino mixing) will combine the benefits of the high resolution of the spectrometer as well as the luminosity and the stability of the WGTS of the KATRIN experiment with a modified detector for a search for sterile neutrinos [14]. The kink-like signature of sterile neutrinos in the beta decay spectrum will be explained in subsection 1.3.1, before a short overview of the measurement principle and the new detector requirements will be given in subsection 1.3.2.

### 1.3.1 Signature of a sterile neutrino on the beta decay spectrum

In section 1.2.2, the influence of an active neutrino mass on the beta decay spectrum was shown. As the effective neutrino mass is assumed to be small, this effect will be observed close to the endpoint energy of tritium. The TRISTAN project will search for a sterile neutrino with a mass of order  $\mathcal{O}(\text{keV})$ . Analogous to equation (1.3), a distortion akin to the effect of the effective neutrino mass will be observed at an energy of  $E_{\text{kink}} = E_0 - m_{\nu, \text{sterile}}$ . The tritium spectrum is a superposition of the decay branch in an active neutrino and the decay branch in a sterile neutrino. The decay in a sterile neutrino stops at  $E_{\text{kink}}$  due to energy conservation, resulting in a kink-like signature in the spectrum, as seen in figure 1.4.

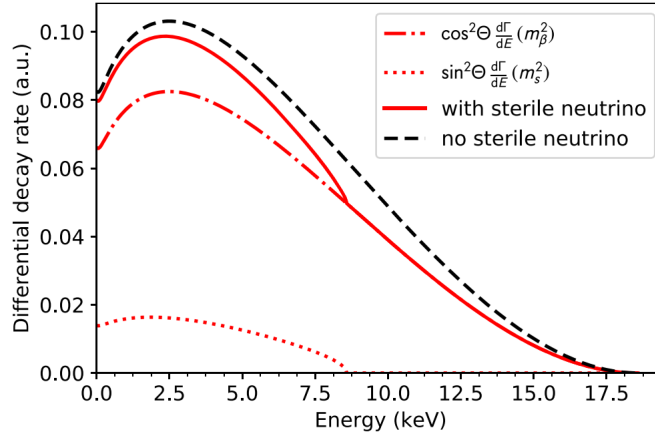


Figure 1.4: Hypothetical beta decay spectrum with a sterile neutrino of mass  $m_{\nu, \text{sterile}} = 10 \text{ keV}$  and a mixing angle of  $\sin^2 \theta = 0.2$ . For a better visibility of the signature of a sterile neutrino, the mixing angle is chosen too large. The decay branches in a sterile neutrino and in an active neutrino are displayed by the red dotted and red dashed-dotted line respectively. The kink-like signature at  $E_{\text{kink}} = E_0 - m_{\nu, \text{sterile}}$  is clearly visible in the superposition of the two decay branches, depicted by the solid red line. The shape of the spectrum with no sterile neutrino is shown by the dashed black line. [15].

### 1.3.2 Detector requirements

Because the range of sterile neutrino mass is unknown, the beta decay spectrum has to be scanned over a broad range of energies in order to find the kink-like signature described in section 1.4. Therefore, the TRISTAN project will use differential mode measurements in addition to integral mode measurements. Being able to use both measurements reduces systematic uncertainties. In integral mode, the retarding potential of the MAC-E-Filter is varied in order to scan over an energy range [14]. In differential mode, the retarding potential is set to a low value, allowing electrons with a wide energy range to reach the detector, which then has to determine the energy of the electrons with the best possible resolution [10]. This results in count rates up to  $10^8$  counts per second for the whole detector system, which the current KATRIN detector is not suited for. Therefore the TRISTAN project has to develop a new detector capable of handling such high rates. Another requirement is an excellent energy resolution so that the small kink-like signature is visible in the spectrum. This can only be achieved with a detector with low noise. A high linearity as well as a clear understanding of the detector response, charge sharing effects and noise behaviour are also crucial [15].

To understand the noise behaviour, this work will focus on the investigation of the noise performance of the current TRISTAN detector prototype. For this purpose, the noise density in the frequency domain as well as the resulting energy resolution in the time domain will be analysed. The results will be compared to those of a detector of the previous generation as well as one detector of the same generation. The final TRISTAN detector system will replace the focal plane detector of the KATRIN experiment described in section 1.2.2. It will consist of approximately 3500 hexagonal silicon drift detector pixels with a diameter of 3mm, grouped together in 21 detector modules with 166 pixels each [15]. A scheme of the final TRISTAN detector system is shown in figure 1.5.

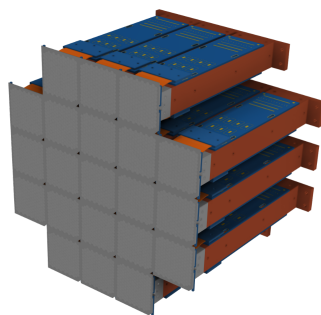


Figure 1.5: Scheme of the final TRISTAN detector system with 21 rectangular modules. Each module consists of 166 silicon drift detector pixels with 3mm diameter, resulting in a total of 3486 pixels for the whole detector.

## Chapter 2

# TRISTAN prototype detector setup

As discussed in section 1.3.2, there are two big challenges the TRISTAN detector has to face: high count rates of about  $10^8$  counts per seconds for the whole detector system and a low noise contribution, resulting in an excellent energy resolution [15]. Furthermore, a large detector area is desirable in order to minimize the effects of charge sharing. These requirements are met by a Silicon Drift Detector, which will be introduced in section 2.1. The experimental setup for the following analysis will be described in section 2.2 before giving an overview of the relevant noise theory in section 2.3.

### 2.1 Working principle of a Silicon Drift Detector

Silicon Drift Detectors (SDD) are used for the TRISTAN project, as they are able to deal with high count rates and possess a small anode relative to the detector area. The latter reduces the noise produced by the detector which in turn improves the detector resolution.

SDDs are semiconductor devices with a slightly temperature dependent pair creation energy of  $E_{\text{pair}} = 3.65$  eV at room temperature and  $E_{\text{pair}} = 3.67$  eV at  $-30^\circ\text{C}$  [16]. When the detector is depleted by an applied bias, an interacting ionizing particle with an energy higher than  $E_{\text{pair}}$  excites electrons from the valence band into the conduction band, leaving holes that act like free positive charges behind. The amount of created charges depends on the energy of the ionizing particle [17].

Figure 2.1 shows the structure of an SDD. A small anode at the center of the device is surrounded by p+ doped drift rings. The negative potential of the drift rings increases from the center outwards, creating an electric field across the whole device and guiding electrons to the collecting anode. Therefore, the whole volume is sensitive to ionizing particles, except for an unavoidable dead layer at the entrance window side, where not all of the deposited energy is collected. If the device has an integrated JFET, it is located in the middle of the device, surrounded by the anode [18].

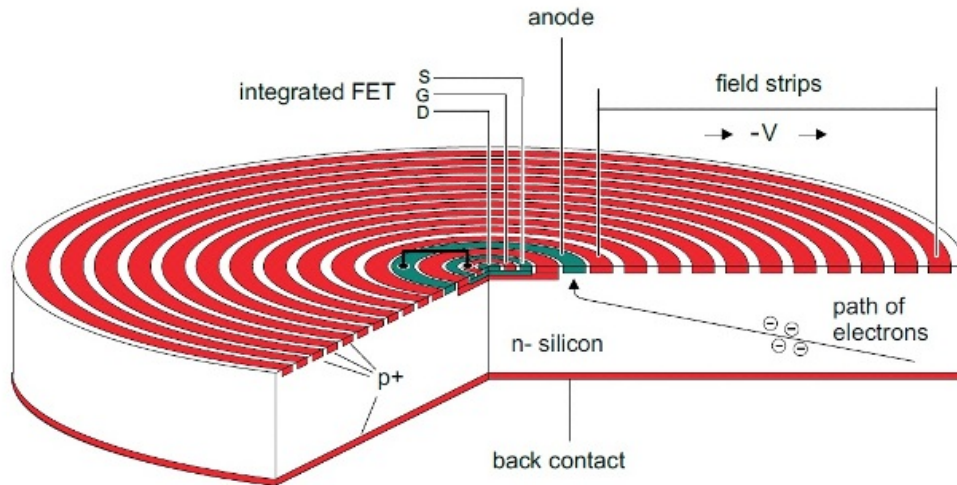


Figure 2.1: Structure of a Silicon Drift Detector. The p+ doped drift rings are depicted in red. They create an electric field in the detector, guiding the electrons to the collecting anode, shown in green. The optional integrated JFET is visible in the middle of the device, surrounded by the anode. [17].

## 2.2 Experimental setup

### 2.2.1 Test stand

All of the following measurements were taken at the MPP test stand. The signal line consists of the detector board, a bias board, the voltage supply, the DANTE **D**igital **P**ulse **P**rocessor (DPP) and a PC, where the measured data is saved. Figure 2.2 shows the components operated in a vacuum chamber. The ambient devices are displayed in figure 2.3.

The detector board is installed in the vacuum chamber, as is the source, in this case,  $^{55}\text{Fe}$ . For measurements below  $0^\circ\text{C}$ , vacuum is necessary to prevent the humidity in the air to freeze on the detector. With the available vacuum pump and the chiller, pressures of  $10 \cdot 10^{-7}$  mbar and temperatures of  $-30^\circ\text{C}$  can be achieved [10].

The detector board itself consists of a **P**rinted **C**ircuit **B**oard (PCB), on which the 7-pixel detectors are attached. Depending on the type of detector, each pixel either has an integrated JFET in the SDD accompanied by an ETTORÉ pre-amplifier or just a CUBE pre-amplifier mounted on the PCB. Both amplify the acquired signal in order to minimize loss of signal, which would lead to a worsened resolution. The detector board is connected to the bias board, which is powered by a voltage supply. It amplifies the signal further as well as keeps the pixels synchronized by performing

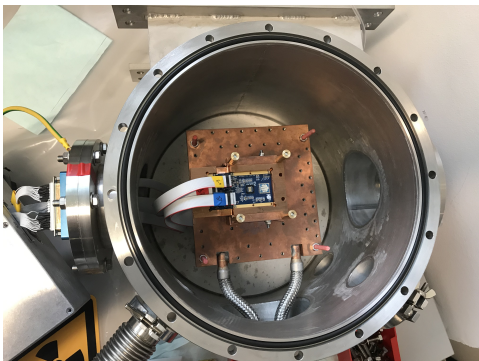


Figure 2.2: PCB with S0-7-1 detector inside of the vacuum chamber. The source is located under the copper plate so that the emitted x-rays can reach the entrance window of the detector.

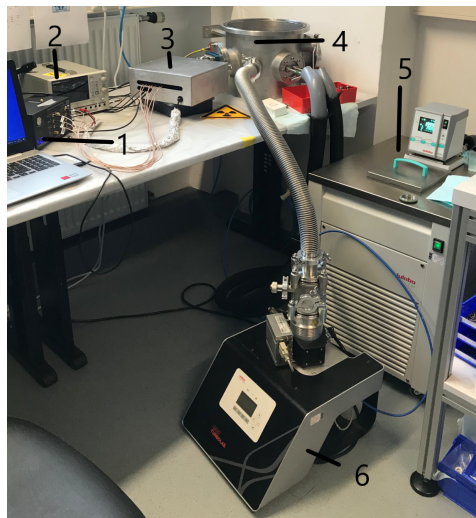


Figure 2.3: General setup of the test stand. 1: DANTE DPP, 2: Voltage supply, 3: Bias Board, 4: Vacuum chamber with detector and source inside, 5: chiller, 6: vacuum pump.

collective resets of all pixels. The bias board also supplies the voltages for the drift rings of the detector. The amplified signal is converted from an analog signal to a digital one in the DANTE DPP, provided by XGLab.

The DANTE DPP provides different modes for the data acquisition. The four modes used for the following measurements are discussed briefly:

- In **waveform mode**, the entire waveform is saved, allowing for analysis of signal rise time, noise spectral density and more.
- In **list wave mode**, a wave snippet containing one event is saved for each event, as well as the time information and the energy output of the trapezoidal filter implemented in the DANTE DPP.
- In **spectrum mode**, the wave snippets are convolved with a trapezoidal filter with one pre-selected peaking time. Only the histogram of the ADC bin amplitudes is saved, while time information is lost.
- The **sweep** is analog to spectrum mode, but instead of having a spectrum at only one peaking time, a spectrum for each peaking time specified in the

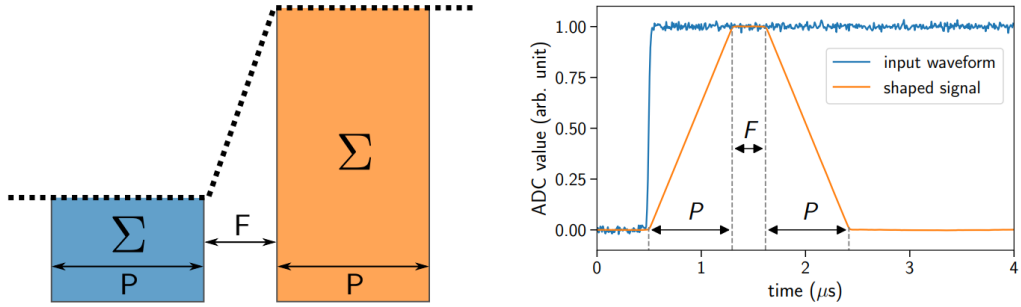


Figure 2.4: Left: Working principle of a trapezoidal filter. The waveform, represented by the black dots, is averaged in two windows. The width of both windows is determined by the peaking time and the windows are separated by the gap time. For a working trapezoidal filter, the minimal value of the gap time is equal to the rise time of the signal. The average of both windows are then subtracted, leading to the characteristic trapezoidal shape of the output. Right: Response of the trapezoidal filter. Adapted from [19].

DANTE Graphic User Interface (GUI) is taken. The gap time does not change and remains constant at  $0.224 \mu\text{s}$ .

The DANTE DPP uses two trapezoidal filters for the determination of the energy of the detected events. The first one is called fast filter and distinguishes the actual events from the noise via a set threshold. These events are then passed to the second trapezoidal filter, the energy filter, to evaluate the energy of the event. The principle of a trapezoidal filter is shown in figure 2.4. The trapezoidal filter averages the digitized waveform over the peaking time and subtracts the first averaged value from the second, which is separated by the gap time from the first. The gap time has to be at least the signal rise time in order to guarantee a well-performing trapezoidal filter with the correct energy output of the event. The optimal peaking time is obtained by considering the detector requirements as well as the influence of the noise contributions on the energy resolution, see section 4.1.

### 2.2.2 TRISTAN detector prototypes

Since the main goal of this work is the comparison of different TRISTAN detector prototypes, the three detectors used for the measurements are addressed briefly. All of them consist of 7 hexagonal pixels in order to enable an arrangement without gaps and therefore without any area insensitive to ionizing particles between the pixels. Figure 2.5 shows the design of the 7-pixel detector. For an easier association, the

central pixel is called Slave 1 in the following analysis. Slave 1 is surrounded by the Master pixel as well as Slave 2 to 6.

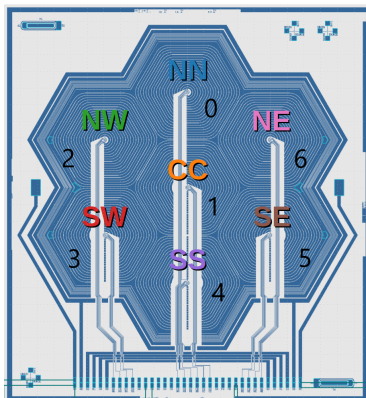


Figure 2.5: Map of the Pixels of all three seven pixel detectors. For an easier association, the nomenclature of the pixels was changed. The central pixel (CC) is called Slave 1 and is surrounded by the Master pixel (0) and Slave 2 to 6. Note that the traces that lead from the anode in the middle of the pixels to the detector board are only present on the S0-7-1 and S0-7-2 detectors. For the S0-1 detector, wire bonds lead from the anode of each pixel to a CUBE amplifier on the detector board.

- **S0-1:** The S0-1 is a detector of the prototype-0 generation. It is the predecessor of the currently used detector. It consists of a SDD without integrated JFET. Instead, the signal is pre-amplified by a CUBE pre-amplifier [20], provided by XGLab and attached to the PCB. Each pixel has a diameter of 2 mm and has its own CUBE pre-amplifier. The S0-1 sets the expectations for the new detector prototypes with a low noise density in the region of  $2 \cdot 10^5 - 2 \cdot 10^7$  Hz and an energy resolution of  $\Delta_{\text{FWHM}} \approx 140$  eV for 6 keV x-rays [15]. As this prototype was already characterized in different works (e.g. [10], [21]), it is only used for comparison in this work.
- **S0-7-1 and S0-7-2:** The detectors of the current detector prototype are called S0-7-1 and S0-7-2. They follow the same design, both are 3 mm in diameter and have an integrated JFET. The ETTORÉ pre-amplifier mounted on the detector board replaces the CUBE pre-amplifier of the S0-1 detector. Figure 2.6 shows the S0-7-2 detector on the PCB. The 7 pixels can be seen at the left hand side of the PCB. Each anode is connected to the PCB. The structure of the S0-7-1 detector is identical.

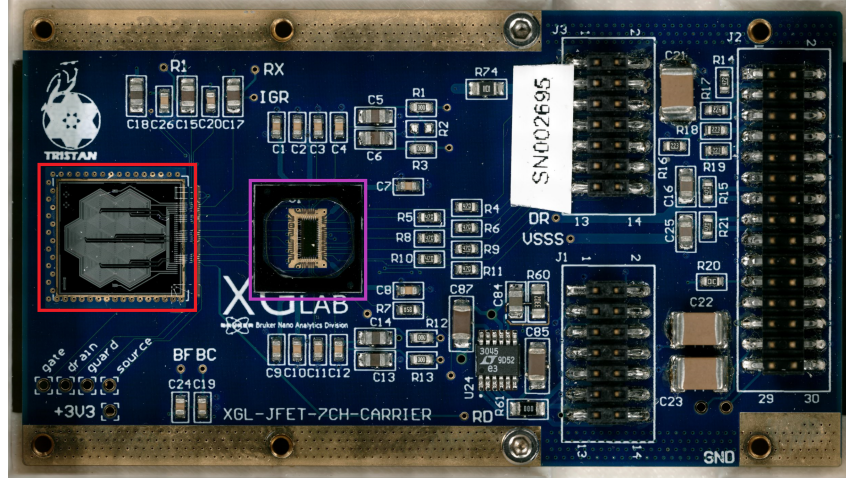


Figure 2.6: PCB of the S0-7-2 detector. The 7 pixels of the detector are marked by the red rectangle. From the anode in the middle of each pixel, connections lead to the PCB, directing the signal to the ETTORE ASIC highlighted in purple.

### 2.2.3 $^{55}\text{Fe}$ source

For all of the following measurements, a  $^{55}\text{Fe}$  source was used.  $^{55}\text{Fe}$  has a half life of 2.747 years and decays by electron capture to  $^{55}\text{Mn}$ . Three emitted x-rays are of interest, shown in table 2.1.

Table 2.1: X-ray energies of the decay of  $^{55}\text{Fe}$  suited for measurements [22].

	Energy (keV)	relative probability
Mn- $K_{\alpha 1}$	5.898 75	0.51
Mn- $K_{\alpha 2}$	5.887 65	1
Mn- $K_{\beta}$	6.490 45	0.205

Even with the high energy resolution of the detectors used in the TRISTAN project, the Mn- $K_{\alpha 1}$ -line and the Mn- $K_{\alpha 2}$ -line are not separated in the spectrum. Therefore they will be considered and treated as one Mn- $K_{\alpha}$ -peak with an energy of approximately 5.89 keV in the following analysis. As the Mn- $K_{\alpha}$ - and Mn- $K_{\beta}$ -line are only about 0.6 keV apart, they provide an opportunity to estimate the energy resolution by eye by how clearly they are separated. Figure 2.7 shows a spectrum measured with the S0-7-1 detector at room temperature at a peaking time of 3.008  $\mu\text{s}$ . The Mn- $K_{\alpha}$ - and Mn- $K_{\beta}$ -peaks are easily distinguishable. The additional, manually inserted noise peak is located at 0 keV.

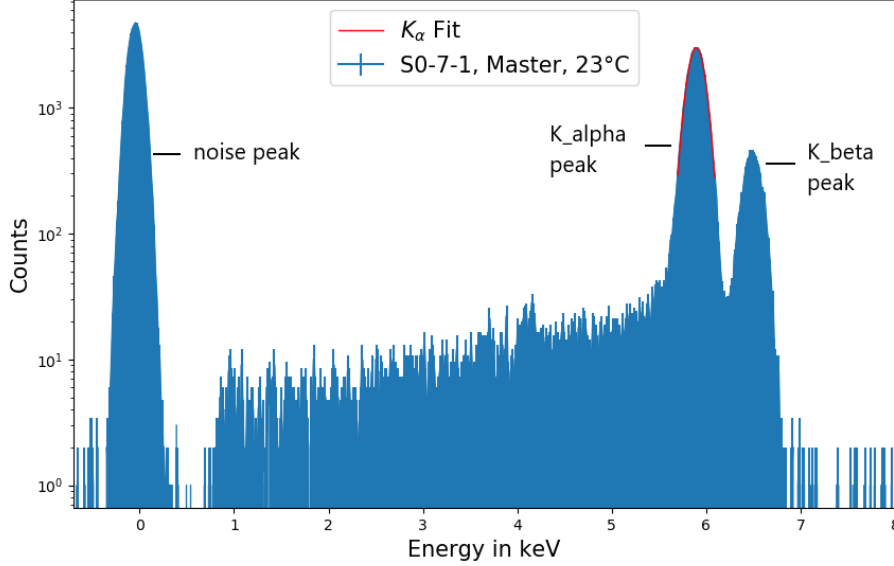


Figure 2.7: Calibrated  $^{55}\text{Fe}$ -spectrum with additional noise peak manually inserted. The spectrum was taken with the S0-7-1 detector at a peaking time of  $3.008\ \mu\text{s}$ . The Mn- $K_\alpha$ - and the Mn- $K_\beta$ -peaks are clearly separated. An exemplary Gaussian fit is applied to the Mn- $K_\alpha$ -peak, depicted in red.

## 2.3 Noise components

### 2.3.1 Fano limit

While noise is usually discussed in terms of minimizing the noise contributions in order to get the best possible energy resolution, there is one inevitable limit to the noise reduction: the Fano limit. The Fano limit describes fluctuations of the charge cloud generated by an ionizing particle in a semiconductor. Along with the electronic noise, it results in a broadening of the Gaussian peaks in the spectrum by  $\sigma^2 = \sigma_{\text{Fano}}^2 + \sigma_{\text{noise}}^2$  [10], [23].  $\sigma_{\text{Fano}}$  is dependent on the Fano Factor  $F$ , the energy  $E$  of the ionizing particle and the pair production energy  $E_{\text{pair}}$  of the semiconductor material [24], as shown in equation (2.1).

$$\sigma_{\text{Fano}}^2 = F \cdot E \cdot E_{\text{pair}}. \quad (2.1)$$

The Fano Factor itself is slightly temperature dependent, but is considered a constant  $F = 0.117$  for the following analysis [16].

Since it can not be changed significantly, the Fano limit is the theoretical limit of noise minimization in a detector.

### 2.3.2 Electronic noise sources

There are two main sources of electronic noise: the shot noise and the thermal noise. The shot noise describes the influence of the leakage current  $I$  of a pn-junction on the signal. The input power spectral density [24] can be written as

$$W_{\text{shot}} = 2eI. \quad (2.2)$$

Thermal noise, also known as Johnson noise, results from velocity fluctuations of the charge carriers in resistors. The input power spectral density amounts to

$$W_{\text{thermal}} = 4k_{\text{B}}TR, \quad (2.3)$$

with the Boltzmann constant  $k_{\text{B}}$ , the temperature  $T$  and the resistance  $R$  [25].

### 2.3.3 Noise in a charge sensitive pre-amplifier

To calculate the effective noise in a charge sensitive pre-amplifier, the response function  $H(\omega)$  of the charge sensitive pre-amplifier is needed. The response function is defined as the ratio of output power spectrum to input power spectral density [26]:

$$H(\omega)^2 = \frac{W_{\text{out}(\omega)}}{W_{\text{in}(\omega)}}. \quad (2.4)$$

This can be calculated over the circuit diagram of a charge sensitive pre-amplifier. For that, noise sources in the circuit diagram have to be considered. In a charge sensitive pre-amplifier these are the shot noise from the detector leakage current, the thermal and  $\frac{1}{f}$  noise of the JFET and the thermal noise from the current source. Multiplying the response function for each of the noise sources with the respective input power spectral density, see equations (2.2) and (2.3), results in a total output noise power of

$$W_{\text{out}}(f) = \underbrace{\frac{2eI}{(2\pi)^2 f^2}}_{\text{current noise}} + \underbrace{C^2 \cdot \frac{A_f}{f}}_{\frac{1}{f}\text{-noise}} + \underbrace{4C^2 k_{\text{B}}T \cdot \left( \frac{a_n}{g_m} + \frac{1}{g_m^2 R} \right)}_{\text{voltage noise}}. \quad (2.5)$$

The transconductance  $g_m$  is material dependent,  $A_f$  describes a device specific  $\frac{1}{f}$ -coefficient of order  $10^{-10} - 10^{-12} \text{ V}^2$  and  $a_n = \frac{2}{3}$  for FETs as used in the TRISTAN project [27], [28].

Note, that the unit of the noise power is given in  $\frac{\text{dENC}^2}{df}$ , where ENC stands for

equivalent noise charge. It describes the amount of charge needed to reproduce the signal made by noise [23] and is calculated by

$$\text{ENC} = \frac{\sigma_{\text{noise}}}{E_{\text{pair}}}. \quad (2.6)$$

While equation (2.5) applies for noise studies in the frequency domain, it is also possible to look at the noise in the time domain. For this purpose, the Fourier transform of the response function  $H(\omega)$  is used, resulting in equation (2.7) [28]:

$$W_{\text{out}}(\tau) = \underbrace{\frac{A_1 \cdot 2eI \cdot \tau}{(2\pi)^2}}_{\text{current noise}} + \underbrace{A_2 \cdot C^2 \cdot A_f}_{\frac{1}{f}\text{-noise}} + \underbrace{A_3 \cdot 4C^2 k_B T \cdot \left( \frac{a_n}{g_m} + \frac{1}{g_m^2 R} \right) \cdot \frac{1}{\tau}}_{\text{voltage noise}}. \quad (2.7)$$

Here, the noise power is given in  $\text{ENC}^2$  and is dependent on the peaking time  $\tau$ . The noise in both the frequency domain as well as the time domain contains three noise components: the current noise, the voltage noise and the  $\frac{1}{f}$  noise. In the time domain, the current noise is proportional to the peaking time, as the leakage current is no longer negligible for long peaking times. The voltage noise however is averaged out for long peaking times, therefore decreasing with  $\tau$ . The  $\frac{1}{f}$ -component is independent of the peaking time, thus constant over all frequencies [10]. The coefficients  $A_1$ ,  $A_2$  and  $A_3$  have to be calculated for each pulse shaper separately by integrating over the squared response function of the pulse shaper:

$$\begin{aligned} A_1 \cdot \tau &= \int_0^{\infty} \frac{1}{f^2} |H_{\text{pulse shaper}}(\omega)|^2 df \\ A_2 &= \int_0^{\infty} \frac{1}{f} |H_{\text{pulse shaper}}(\omega)|^2 df \\ \frac{A_3}{\tau} &= \int_0^{\infty} |H_{\text{pulse shaper}}(\omega)|^2 df. \end{aligned} \quad (2.8)$$

For a trapezoidal filter with  $\tau_{\text{gap}} = 0.2 \cdot \tau$ , the coefficients are displayed in table 2.2.

Table 2.2: Calculated noise coefficients for current, voltage and  $\frac{1}{f}$  noise for a trapezoidal filter with  $\tau_{\text{gap}} = 0.2 \cdot \tau$

Coefficients	Values
$A_1$	17.1
$A_2$	3.23
$A_3$	1.00

# Chapter 3

## Noise density measurements

To investigate the noise performance of the TRISTAN detectors, the analysis of the noise spectral density is suited, as it contains valuable information about the physical parameters while illustrating the results in an understandable manner. In section 3.1, the preparation of the waveform necessary to obtain the noise spectral density is described. The S0-7-1 detector is characterized in section 3.2 and is compared to other detectors of the TRISTAN project in section 3.3. Lastly, the temperature dependence of the noise spectral density of the S0-7-2 detector will be examined in section 3.4.

### 3.1 Waveform preparation

All of the following analyses are performed on waveform data taken with the DANTE DPP. A part of the waveform used for the S0-7-2 detector is shown in figure 3.1. Except for the exact value of the slope of the ramp which is proportional to the leakage current, the waveform looks similar for all three detectors covered in this work. To get the noise spectral density, the waveform is Fourier transformed into the frequency domain. The resets and events in the waveform would distort the noise spectral density. For this reason, snippets without resets or events are used.

In order to get information about a wide range of frequencies down to low frequencies, the snippets of the waveform have to be as long as possible. The maximal length of the snippets is the length of the ramp. The slope of the ramp is influenced by the leakage current. The steeper the slope of the ramp, the earlier the reset. Therefore, a higher leakage current leads to shorter waveform snippets without events and resets. The leakage current is dependent on the temperature and the detector prototype. For this reason, different lengths of waveform snippets are used for the different generations of TRISTAN detectors. The snippets used for the S0-7-1 and S0-7-2 detector are 2.24 ms long for each temperature. Due to the higher leakage current of the S0-1 detector, only 0.256 ms long snippets can be extracted for the old generation. The obtained snippets are then Fourier transformed into the frequency domain and averaged in order to obtain the noise spectral density of the detectors.

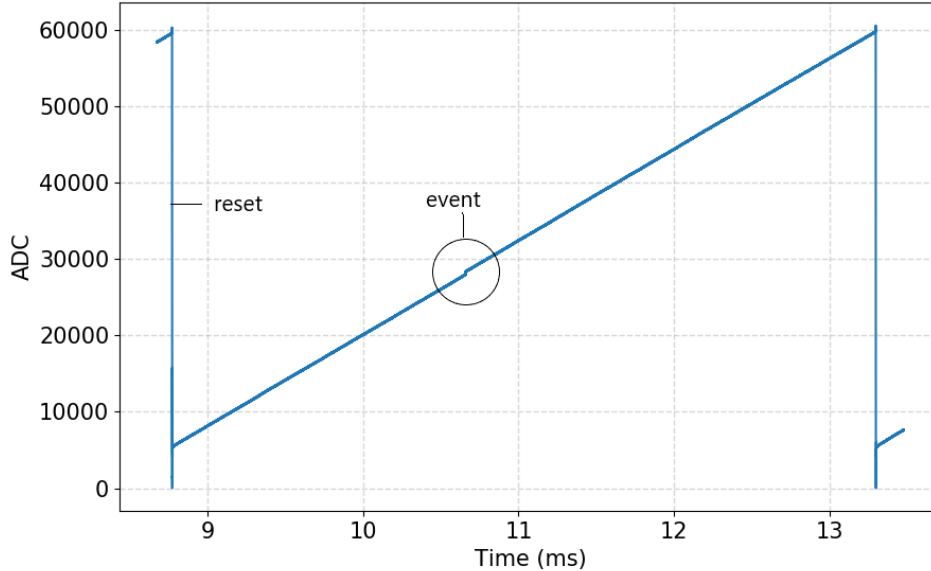


Figure 3.1: Exemplary waveform of the S0-7-2 detector at 23 °C. The event is circled. At the beginning and the end of the ramp the resets are located. The slope of the ramp is proportional to the leakage current.

### 3.2 Noise density spectrum of the S0-7-1 detector

The noise spectral density is expected to follow roughly the model described by equation (2.5). The model as well as the influence of the different noise components are shown exemplary for the Master pixel at room temperature in figure 3.2. Towards low frequencies, the noise spectral density model is dominated by the leakage current, resulting in a steep increase. At high frequencies, the noise spectral density model is dominated by white noise, hence remaining constant. While the noise density spectrum follows the course of the model for low frequencies, a drop is observed at high frequencies around  $4 \cdot 10^6 - 1 \cdot 10^7$  Hz where the spectrum is expected to remain constant. The observed drop is pixel dependent and correlates inversely with the length of the traces connecting the anode with the detector board, shown in figure 2.6. This correlation is yet to be explained. In regards to the expectations of a low noise density, the drop can also be interpreted as an elevation of the noise density in the region of  $2 \cdot 10^5 - 4 \cdot 10^6$  Hz. Either way the non constant course of the noise density at high frequencies is a hint that the model to describe the noise spectral density is not complete and a noise component is missing. The spikes are also not

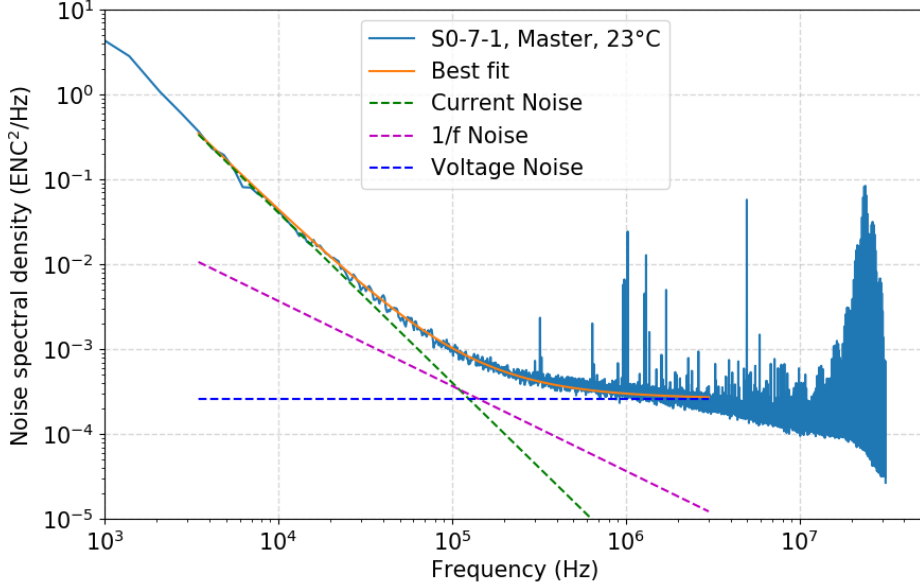


Figure 3.2: Fit to the noise spectral density of the Master pixel of the S0-7-1 detector at room temperature. The green dashed line represents the current noise, which dominates the spectrum at low frequencies. The magenta dashed line shows the influence of the  $\frac{1}{f}$  noise while the blue dashed line illustrates the white noise. The spikes as well as the region at high frequencies, where the drop is located, are not accounted for in the model and thus not considered for the fit. The fit is shown with the solid orange line and fits the measurement well.

included in this model, as they originate from the bias board, which is different for different detector generations. However, the model is sufficient for the purpose of this work.

From the fit, physical parameters such as the leakage current  $I$ , the capacitance  $C$  as well as the  $\frac{1}{f}$ -coefficient are extracted. At room temperature, the transconductance amounts to  $g_m = 150 \frac{\mu\text{A}}{\text{V}}$  [29]. The fitted parameters are shown in table 3.1, along with the expectations for the parameters. Except for the capacitance  $C$ , they match. The extracted fit value for the capacitance however is larger than expected.

The value of the capacitance was investigated in different tests, which exclude the possibility of an increased capacitance. This hints at another noise source currently unknown, that manifests itself in the used model as an enlarged capacitance.

The noise density spectrum for all pixels of the S0-7-1 detector at room temperature is shown in figure 3.3. A similar performance following the course of the model

Table 3.1: Physical values for the leakage current, the  $\frac{1}{f}$ -coefficient and the capacitance extracted from the fit of the noise spectral density. The fitted measurement was taken with the Master pixel of the S0-7-1 detector at 23 °C. Except for the capacitance  $C$ , the values fall within the expected range [30].

	I (pA)	C (fF)	H (V <sup>2</sup> )
Best fit	$12.85 \pm 0.02$	$303 \pm 6$	$1.03 \pm 0.07 \cdot 10^{-11}$
Expectation	10	190	$10^{-12} - 10^{-11}$

is expected for all seven pixels. Except for Slave 3, the pixels of the S0-7-1 are homogeneous. Slave 3 however shows a strange behaviour at a frequency range of  $7 \cdot 10^4 - 1 \cdot 10^6$  Hz, where the noise density is higher than for the other pixels.

### 3.3 Noise density of different detectors

To gain more insight in the noise behaviour, the S0-7-1 detector is compared to the S0-1 detector, a detector of a previous generation, in subsection 3.3.1. To test if the elevated noise density is a common issue to all detectors of the new generation, a comparison between two detectors of the same generation is performed in subsection 3.3.2.

#### 3.3.1 Comparison of different generations of detectors

As described in section 2.2, the detectors of different generations, in this case the S0-7-1 and the S0-1 detector, follow the same principle but have a different structure. The setup of the bias board is different, therefore it is expected that both detectors have different spikes in their noise density spectra. The model for both remains the same, so the spectra are assumed to be similar.

Figure 3.4 shows the comparison of the noise density spectra of the S0-7-1 detector and the S0-1 detector at room temperature. For this analysis, the noise density of all pixels of each detector is averaged. Note that of the seven pixels of the S0-1 detector, only five were working at the time of the measurement.

The course of the noise densities of the S0-1 and S0-7-1 detector is different. The S0-1 detector follows the course of the model. At low frequencies, a steep decline is visible, before the noise density flattens. For high frequencies the noise density remains approximately constant. The S0-7-1 however shows a drop at the end of the spectrum. This indicates that the model does not describe the noise behaviour of the S0-7-1 accurately, meaning that there may be another noise component previously not considered.

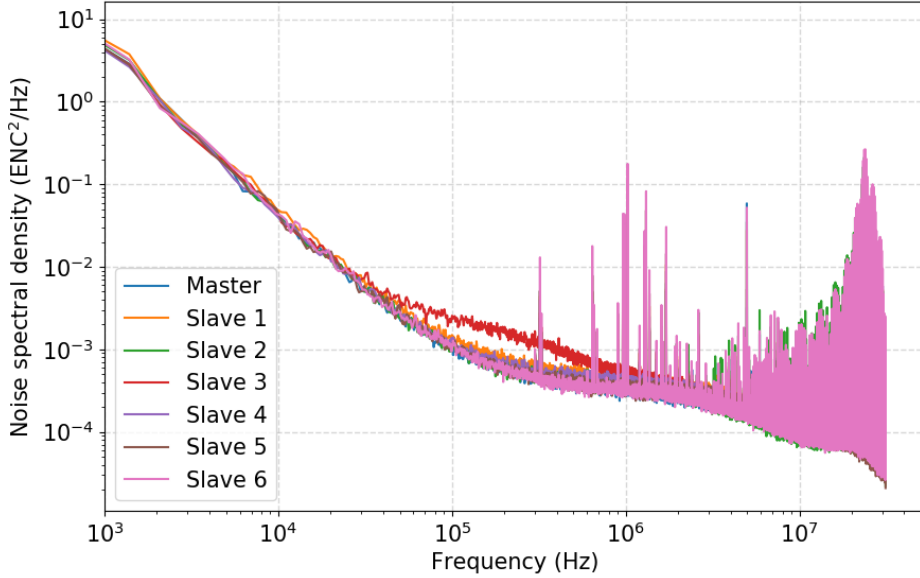


Figure 3.3: Noise spectral density for all pixels of the S0-7-1 detector at room temperature. The pixels are homogeneous except for Slave 3 at a frequency range of  $7 \cdot 10^4 - 1 \cdot 10^6$  Hz, where it is considerably higher than the rest of the pixels. The spikes at high frequencies originate among others from the switching power supply on the bias board.

At low frequencies, the noise density of the S0-1 detector is about one order of magnitude higher than for the S0-7-1 detector. This hints at a higher leakage current of the S0-1 detector compared to the S0-7-1 detector. As the current noise is proportional to the leakage current, a smaller value leads to a better energy resolution. At frequencies starting at about  $2 \cdot 10^5$  Hz, the noise density of the S0-1 detector decreases steeper than the S0-7-1, resulting in an significant incongruity of the graphs. The S0-7-1 detector performs about half an order of magnitude poorer than its predecessor. In this region, the spectra are dominated by the voltage noise, which is proportional to the capacitance  $C$ , confirming the observation of a seemingly increased capacitance in section 3.2. The S0-7-1 detector therefore shows a worse noise behaviour, which is translatable into a significantly worse energy resolution. This will be examined more closely in section 4.1.

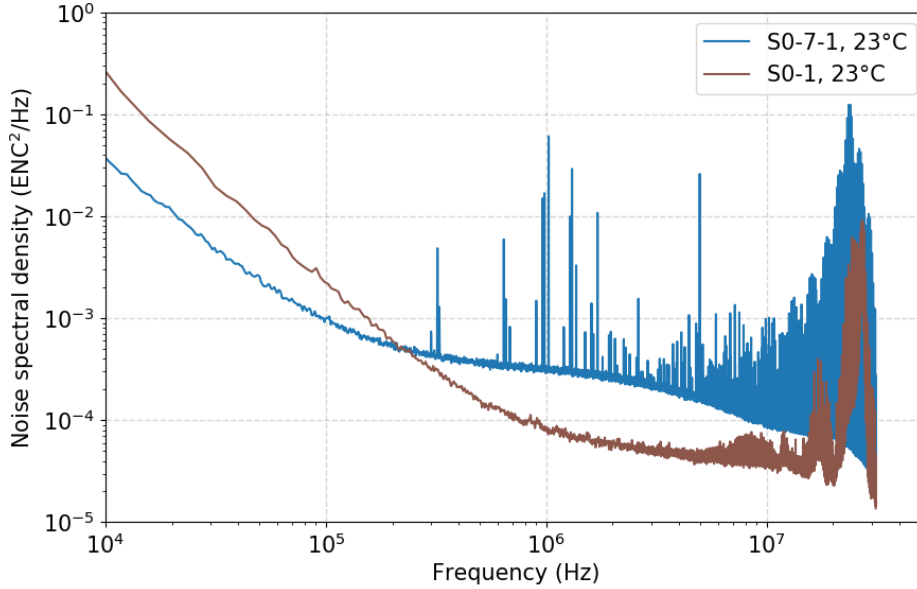


Figure 3.4: Comparison of the averaged noise density spectra of the S0-7-1 detector in blue and the S0-1 detector in brown. The measurements were taken at room temperature. At low frequencies, where the leakage current dominates, a big discrepancy between the generations can be observed. In this region, the S0-7-1 shows a significantly better noise behaviour. At medium and high frequencies however, the S0-1 is located constantly under the S0-7-1 detector, showing fewer noise in this region.

### 3.3.2 Comparison of different detectors of same generation

To rule out a production error, different detectors of the same generation, namely the S0-7-1 and the S0-7-2 detectors are compared at room temperature. Figure 3.5 shows the noise density spectra of both detectors. For this analysis, the average of the pixels for each detector is used. Because Slave 3 of the S0-7-1 detector shows unexpected behaviour, it is not considered in this comparison.

The detectors of the new generation both show a similar noise behaviour. At low frequencies, the noise density of the S0-7-1 detector is slightly higher than for the S0-7-2 detector. Still both noise densities correspond to a similar value for the leakage current for both detectors, as the mismatch is not significant. In the noise densities of both detectors a drop at high frequencies is observed. However, the drop of the S0-7-1 detector is steeper than of the S0-7-2 detector. The spikes of both detectors are similar, which is in agreement with the expectation since the bias board for both

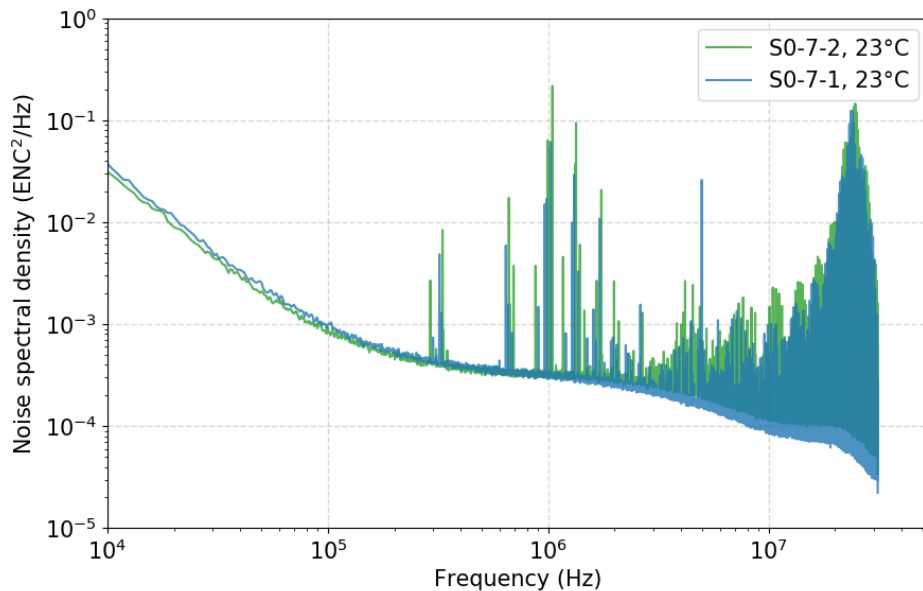


Figure 3.5: Comparison between the detectors of the same generation at room temperature. The noise density of the S0-7-1 detector is depicted in blue, while the S0-7-2 detector is represented by the green line. Both detectors of the new generation show a similar behaviour at all frequencies. No significant mismatch is observed.

detectors is identical.

The similarity between both detectors of the new generation leads to the conclusion, that the elevated noise density is exclusively associated with detectors of the new generation.

### 3.4 Temperature dependence of the noise density spectrum

The final TRISTAN detector is expected to be operated at cold temperatures. In order to evaluate the temperature dependence of the noise density, measurements at temperatures in a range from 23 – –30 °C were taken for the S0-7-2 detector. In subsection 3.3.2 it was shown that the behaviour of the detectors of the new prototype are similar. Therefore this temperature dependence is expected to be comparable for the S0-7-1 detector.

Figure 3.6 shows the obtained noise density spectra for different temperatures for

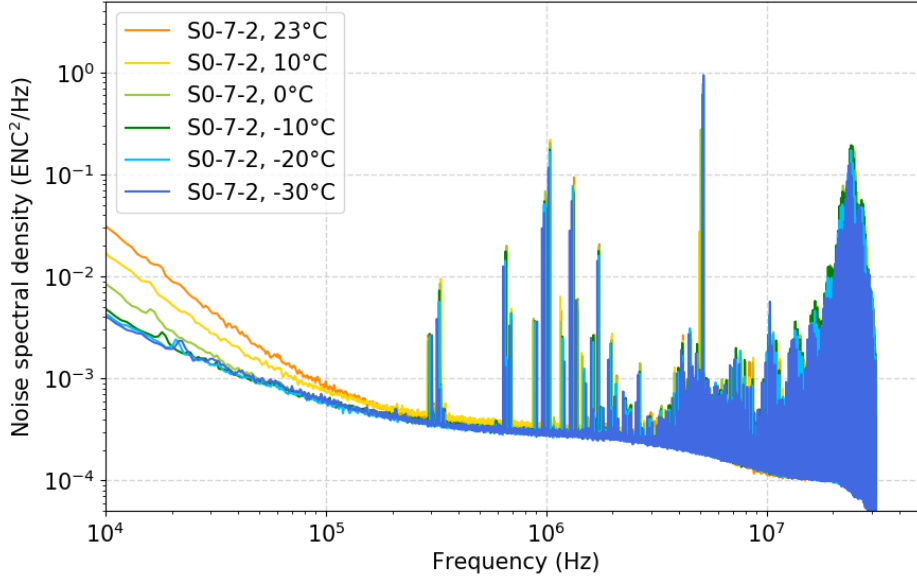


Figure 3.6: Temperature dependence of the noise density of the S0-7-2 detector. The behaviour at low frequencies is clearly temperature dependent as the noise density increases with higher temperature in this region. In the region between  $2 \cdot 10^5$  Hz and  $1 \cdot 10^6$  Hz, a small variation is also observed.

the S0-7-2 detector. The change most visible is the decrease of the noise density at lower frequencies. This change is located in the part of the spectrum which is dominated by current noise. The cause of the current noise is the leakage current, which decreases when the device is cooled. This is in agreement with the expectation of an improved energy resolution at cold temperatures. The noise density also decreases slightly in the part dominated by voltage noise, which is explicitly dependent on the temperature, as seen in equation (2.5).

The exact behaviour of the leakage current for all seven pixels of the S0-7-2 is illustrated in figure 3.7. All pixels follow the expected exponential behaviour. The leakage current appears to be pixel dependent, as especially the Master pixel has a higher leakage current most notably at cold temperatures.

A comparison between the leakage current of the old generation and the new generation is shown in 3.8. The behaviour seen in subsection 3.3.1 is confirmed, as the old generation has a significantly higher leakage current than the S0-7-2 detector at all temperatures.

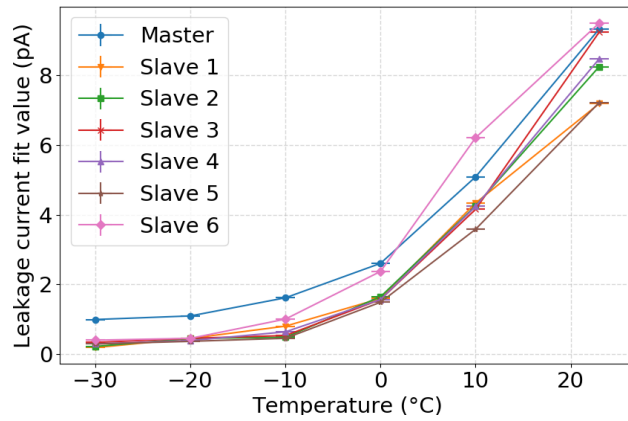


Figure 3.7: Temperature dependence of the leakage current of all seven pixels of the S0-7-2 detector. All pixels follow an exponential behaviour, which is expected. The value of the leakage current is pixel dependent. Especially the Master pixel shows a higher leakage current at cold temperatures than the other pixels.

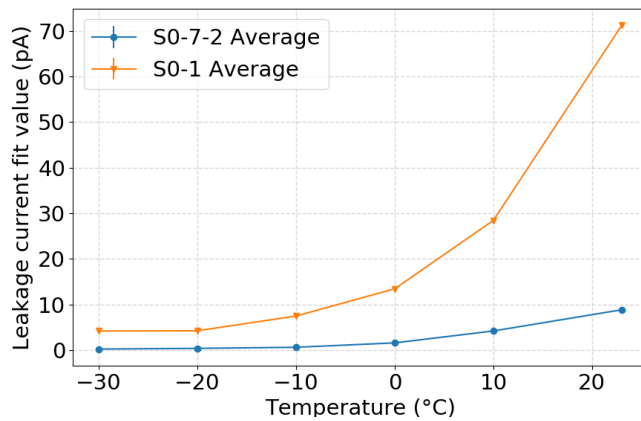


Figure 3.8: Comparison of the average leakage current of the old and the new generation of detectors. The S0-1 detector, depicted in orange, has a higher leakage current at all temperatures than the S0-7-2 detector, shown in blue. Both follow the expected exponential behaviour.



## Chapter 4

# Noise curve measurements and simulations

A more intuitive approach of noise investigation is the analysis of noise in the time domain instead of the frequency domain. In the time domain, the main noise components are dependent on the time constants of the trapezoidal filter, which is responsible for the energy output of the measurements. In section 4.1, this dependency of the energy resolution will be shown in form of a noise curve. To verify the measurements, a simulation will be performed and analysed in section 4.2. The calculated and measured noise coefficients of equation (2.7) are compared and the results of the noise spectral density are cross-checked in section 4.3. For a better understanding of the filter response, the influence of the gap time of the trapezoidal filter on the energy resolution will be investigated in section 4.4. Lastly, the influence of the peaking time on the peak position will be examined in section 4.5.

### 4.1 Energy resolution of the S0-7-1 detector

For the analysis of the energy resolution, a DANTE sweep was taken with peaking times between  $0.16\ \mu\text{s}$  and  $16\ \mu\text{s}$ , resulting in 14 spectra. The gap time remained constant at  $0.224\ \mu\text{s}$  for all values of the peaking time. A linear energy calibration is performed on the resulting spectra. For a detailed investigation of the linearity of the detector, see [31].

After the energy calibration, the Mn- $K_\alpha$ -peak is fitted again with a Gaussian function to determine the FWHM (**F**ull **W**idth **H**alf **M**aximum). A calibrated spectrum with an exemplary fit of the Mn- $K_\alpha$ -peak is illustrated in figure 2.7.

The corresponding ENC values are calculated by subtracting the Fano noise from the determined width of the Gaussian function, as described in equation (2.6)

$$\text{ENC} = \frac{\sqrt{\sigma^2 - \sigma_{\text{Fano}}^2}}{E_{\text{pair}}}. \quad (4.1)$$

Figure 4.1 shows the measured noise curve for all seven pixels of the S0-7-1 detector at  $23\ ^\circ\text{C}$ . The behaviour of all pixels is similar, except for Slave 6 at short peaking times

and Slave 3 at peaking times of  $0.8\text{--}2\ \mu\text{s}$ . Slave 3 shows a worse resolution, which is confirmed by the noise spectral density behaviour examined in section 3.2. The behaviour of Slave 6 indicates a higher voltage noise component at high frequencies, which is not observed in the noise spectral density analysis.

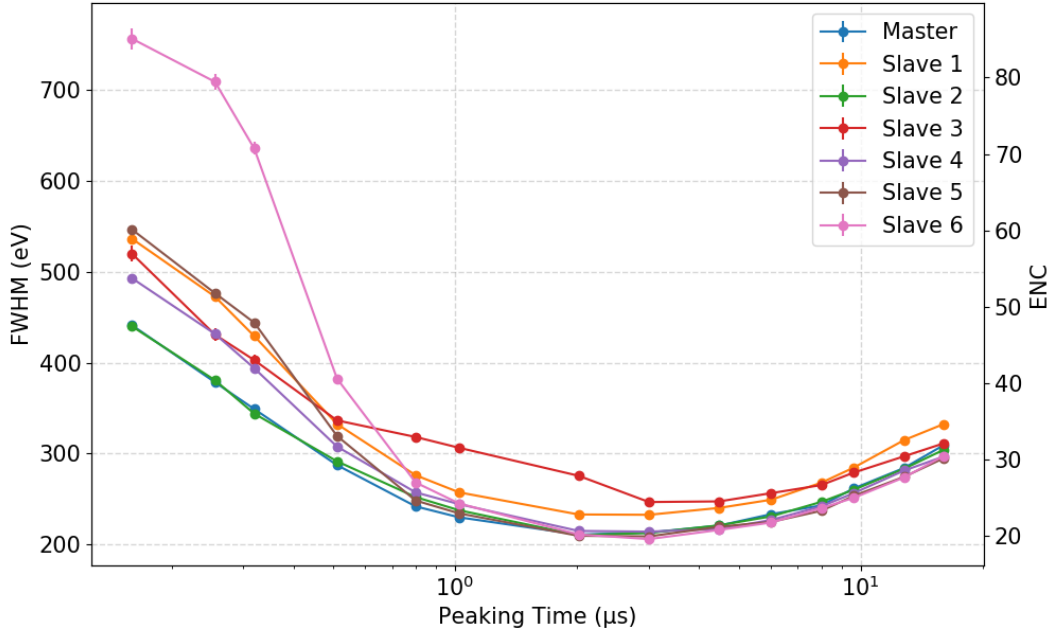


Figure 4.1: Energy resolution of all seven pixels of the S0-7-1 detector at  $23\text{ }^\circ\text{C}$  as a function of the peaking time of the trapezoidal filter. The gap time remains constant at  $\tau_{\text{gap}} = 0.224\ \mu\text{s}$ . The behaviour is, except for Slave 6 at short peaking times and Slave 3 at medium peaking times, similar for all pixels. Slave 3 however has a visibly worse energy resolution at the region of interest at approximately  $1\ \mu\text{s}$ .

The best energy resolution measured at room temperature is  $\Delta E_{\text{FWHM}} \approx 210\ \text{eV}$  for each pixel except Slave 3, which is considerably poorer. This value is higher as expected.

A comparison between the S0-1 and S0-7-1 detector at  $20\text{ }^\circ\text{C}$  and  $23\text{ }^\circ\text{C}$  respectively is shown in figure 4.2. As expected from the noise density measurements in section 3.3.1, the noise curves of the two detectors are different. The S0-7-1 detector shows a worse energy resolution at nearly all peaking times except for very high peaking times, where the higher leakage current of the S0-1 detector dominates and both detectors perform similar. Especially for very low peaking times, where the final TRISTAN detector will be operated, the S0-1 detector excels with an energy resolution of  $\Delta E_{\text{FWHM}} \approx 164\ \text{eV}$ .

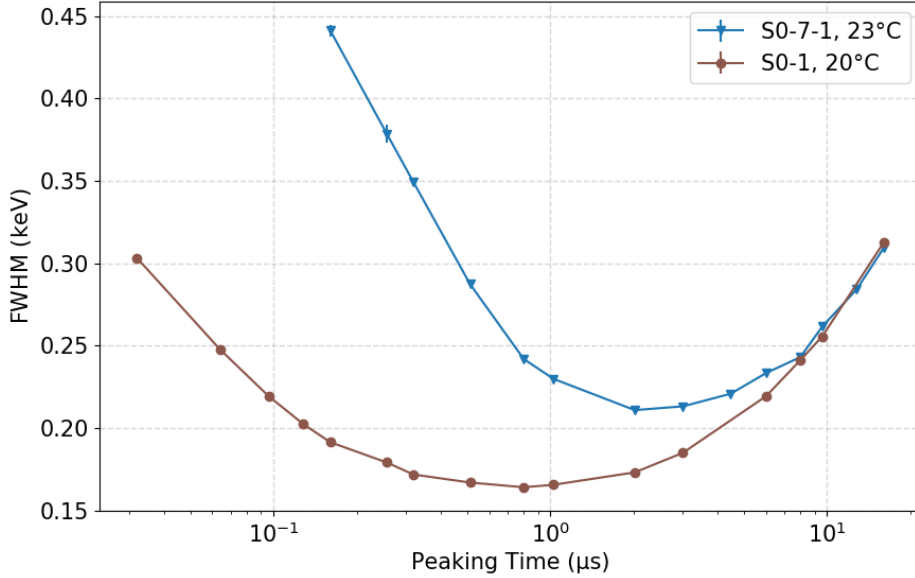


Figure 4.2: Comparison of the noise curve of the S0-1 and the S0-7-1 detector at 20 °C and 23 °C respectively. The S0-1 detector, represented by the brown line, has its minimum at around 1  $\mu\text{s}$  while it is at higher peaking times for the S0-7-1 detector, depicted in blue. Except for long peaking times where the noise curves overlap, the S0-1 detector has a significantly better noise performance than the S0-7-1 prototype.

The comparison of the detector generations confirm the worse energy resolution of the new detector generation, caused by the increased noise seen in section 3.3.1. The S0-7-1 detector therefore does not meet the expectations the S0-1 detector has set. The discrepancy between the different generations is critical, as it is located in the region of interest at low peaking times  $< 1 \mu\text{s}$ .

## 4.2 Verification of measurements with waveform simulation

In order to cross-check the noise spectral density analysis, waveforms corresponding to the fit of the noise spectral densities in section 3.2 are simulated. These waveforms are convolved with a trapezoidal filter, resulting in noise peaks that are translated into the energy resolution. In this section, a comparison of the measured and simulated noise curves of the S0-7-1 detector at 23 °C is performed.

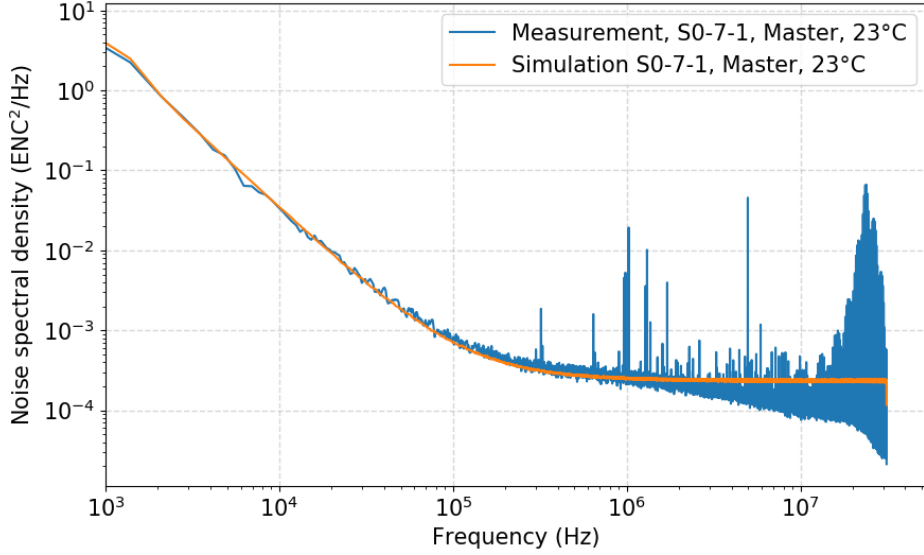


Figure 4.3: Comparison of simulated and measured noise spectral density for the Master pixel of the S0-7-1 detector at 23 °C. The simulation matches the measurement except for the spikes at high frequencies. This is expected to lead to a mismatch of simulation and measurement at short peaking times in the time domain.

**Waveform simulation** For the simulation, random Gaussian distributed noise is generated in the time domain. This white noise is transferred to the frequency domain by a Fourier transform. By multiplying the result with the underlying model, equation (4.2), a simulated noise density spectrum is created. The value of the parameters for the current noise, the  $\frac{1}{f}$  noise and the voltage noise are extracted from the fit of the noise densities, described in section 3.2. The transconductance  $g_m$  is only known for room temperature, therefore the physical values for the capacitance  $C$  and the  $\frac{1}{f}$  coefficient  $A_f$  can not be determined for the measurement at  $-30$  °C. In this case, a simplification of equation (2.5) is used, shown in equation (4.2).

$$\text{ENC}^2 = \frac{A_{\text{cur}}}{f^2} + \frac{A_f}{f} + A_{\text{volt}}. \quad (4.2)$$

For 23 °C, a comparison of the simulation and the measurement in the frequency domain is shown in figure 4.3. The procedure for  $-30$  °C is analogous. The simulation and the measurement match, except for the spikes at high frequencies, as they are not considered in the fit and therefore in the model used for the simulation. This means that a small mismatch of simulation and measurement in the time domain is

expected at short peaking times. As the spikes are different for each bias board and are not constant in time, the effort to include the spikes in the model outweighs the benefits.

The simulated noise density is transformed back into a waveform with an inverse Fourier transform. With this approach, 1500 waveforms are simulated for each temperature. Each of the waveforms is convolved, using a manual trapezoidal filter with variable peaking time and a gap time of  $0.224 \mu\text{s}$ , and the noise peak of each waveform is fitted with a Gaussian function. For the simulated noise curve, the average value of the determined energy resolution of all 1500 simulations is used per peaking time. Note that because no events are simulated the noise peak is fitted. The resulting noise is therefore only of electronic nature.

**Comparison of the simulations and the measurements** Figure 4.4 shows the resulting comparison between simulation and measurement at  $23^\circ\text{C}$  and  $-30^\circ\text{C}$  for the Master pixel of the S0-7-1. The simulation is in agreement with the measurement at  $23^\circ\text{C}$ . At short peaking times a small mismatch is observed, caused by the disregard of the spikes at high frequencies in the model. At  $-30^\circ\text{C}$  however, the mismatch is not limited to short peaking times but remains a constant factor of  $\approx 0.8$  at all peaking times. This can not be explained physically and requires further investigation.

### 4.3 Determination of the noise coefficients of the trapezoidal filter

In order to extract physical values such as the leakage current  $I$ , the  $\frac{1}{f}$ -coefficient  $H$  and the capacitance  $C$  from a noise curve, the noise coefficients  $A_1$ ,  $A_2$  and  $A_3$  of equation (2.7) have to be known. They can be calculated by integrating over the response function of a trapezoidal filter, see equations (2.8). In this case, the ratio of the peaking time  $\tau$  and the gap time  $\tau_{\text{gap}}$  has to be constant. In this section, a noise curve simulation is performed in order to cross-check the calculation of the noise coefficients.

**Cross-check of the calculated noise coefficients with a simulation.** For the cross-check, 1500 waveforms are simulated as described in section 4.2. This time, instead of fitted parameters, the ideal parameters shown in table 4.3 are used for the simulation. Therefore, the physical parameters are known. The procedure to obtain the simulated noise curve is analogous to section 4.2. The relation  $\tau_{\text{gap}} = 0.2 \cdot \tau$  is used for the trapezoidal filter. The noise curve is then fitted with equation (2.7). While

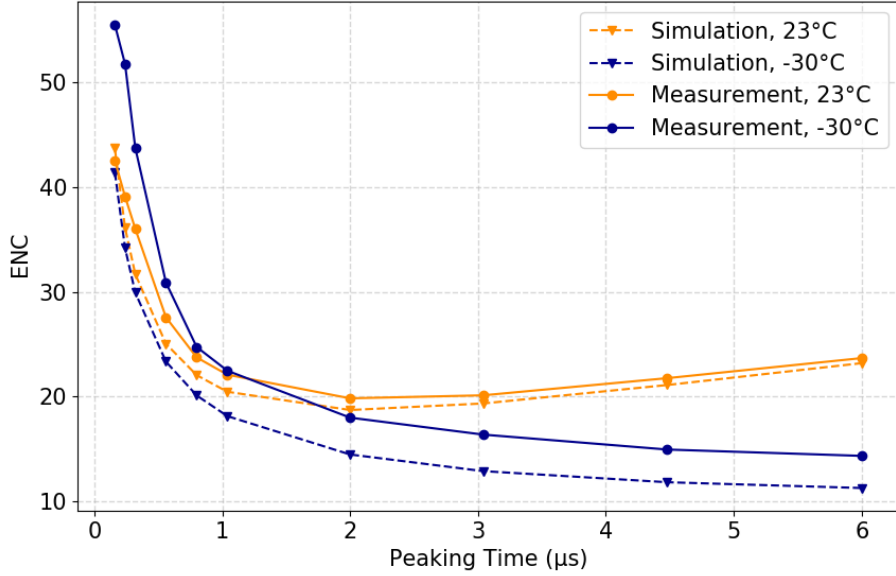


Figure 4.4: Comparison of simulated and measured noise curves of the Master pixel of the S0-7-1 detector. The solid lines in orange and blue describe the measurements at 23 °C and −30 °C, respectively, while the dashed lines of the respective colour show the corresponding simulation. At 23 °C, the simulation is in accordance with the measurement. Small deviations can be seen at short peaking times due to the missing spikes in the simulation. At −30 °C however, there is a constant mismatch between simulation and measurement. The origin of this factor could not be found in the time of this work.

$I$ ,  $H$ ,  $C$  and  $g_m$  are given, the noise coefficients  $A_1$ ,  $A_2$  and  $A_3$  are free parameters. In table 4.1, the noise coefficients extracted from the fit and the calculated noise coefficients are compared. The coefficients for the  $\frac{1}{f}$  noise and for the voltage noise match, while there is a small mismatch for the values for the leakage current. This can be explained by the method used to perform the simulation. The simulation is based on statistically distributed white noise. This means that a small deviation of the given parameters, especially for the leakage current  $I$  is possible. However, for the fit of the noise coefficients, these parameters are assumed to be precisely known. Therefore, a small mismatch is within the range of expectation. The difference between the calculated and the fitted noise coefficients is negligible, as it does not affect the results in a noticeable manner.

Table 4.1: Comparison of calculated noise coefficients and fitted noise coefficients. While  $A_2$  and  $A_3$  match, the values for  $A_1$  are slightly different. This difference is negligible.

	$A_1$	$A_2$	$A_3$
Calculation	17.1	3.23	1.00
Fit value	$17.20 \pm 0.03$	$3.20 \pm 0.02$	$0.9999 \pm 0.0003$

**Determination of physical values with noise coefficients** With the knowledge of the noise coefficients and the transconductance physical values of the leakage current, the capacitance and the  $\frac{1}{f}$ -coefficient are extracted from the measured noise curve. For room temperature, the transconductance amounts to  $g_m = 150 \frac{\mu\text{A}}{\text{V}}$ . The fit values for the physical parameters for the Master pixel of the S0-7-1 detector at room temperature are shown in table 4.2, along with the values extracted from the noise spectral density in section 3.2.

Both methods deliver different values for the leakage current, the capacitance and

Table 4.2: Comparison of the physical values for the leakage current, the  $\frac{1}{f}$  coefficient and the capacitance extracted from the fit of the noise spectral density and the noise curve of the Master pixel of the S0-7-1 detector at 23 °C. The values for the leakage current, the capacitance and the  $\frac{1}{f}$ -coefficient differ.

	I (pA)	C (fF)	H (V <sup>2</sup> )
Noise spectral density	$12.85 \pm 0.02$	$303 \pm 6$	$1.03 \pm 0.07 \cdot 10^{-11}$
Noise curve	$11.10 \pm 0.01$	$351 \pm 3$	$6.05 \pm 0.54 \cdot 10^{-12}$

the  $\frac{1}{f}$ -coefficient, that do not match within uncertainties. As described in section 3.2, the spikes of the noise density spectrum and the drop towards high frequencies disrupt the fit. With a better model describing both noise density spectrum and noise curve, the difference in the extracted values might decrease. Overall, both methods provide a valuable insight into the order of magnitude of the physical values.

To illustrate the issue of the worsened energy resolution of the new detector prototype, a waveform with ideal parameters at room temperature is simulated. The parameters are shown in table 4.3, while the effect is displayed in figure 4.5.

The values are more of an expectation than a strict constraint, but they visualise the influence especially of the capacitance in the region of interest on the energy resolution. The simulation presents a significantly better energy resolution than the measurement, confirming the increased noise of a seemingly too high capacitance of the new generation detectors.

Table 4.3: Expected values for leakage current, capacitance,  $\frac{1}{f}$ -coefficient and transconductance used for a simulation of an "ideal" noise curve [29], [30].

	I (pA)	C (fF)	H (V <sup>2</sup> )	$g_m$ ( $\frac{\mu A}{V}$ )
Ideal values	10	190	$1 \cdot 10^{-11}$	150

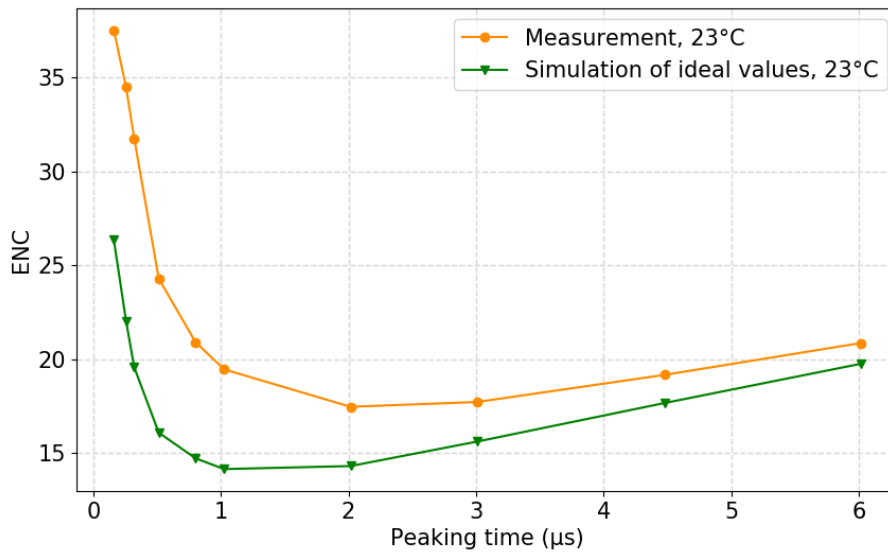


Figure 4.5: Comparison between the measured noise curve, represented by the orange line, and the simulation in green with the expected values for the leakage current, the capacitance, the  $\frac{1}{f}$ -coefficient and the transconductance. Especially in the region of interest at about 1  $\mu s$  peaking time there is a mismatch, resulting in a significantly better energy resolution of the simulation.

## 4.4 Analysis of the influence of the gap time of a trapezoidal filter

In section 4.1, the influence of the peaking time  $\tau$  on the energy resolution was analysed. But not only the peaking time can be changed in a trapezoidal filter, the gap time can also be varied. While in theory the gap time should not influence the energy output of a trapezoidal filter as long as it exceeds the signal rise time [32], it is necessary to test this in order to get the best possible energy resolution. The signal rise time measured with the DANTE DPP at room temperature amounts to  $\tau_{\text{rise}} \approx 53.42$  ns. For a more detailed explanation of the signal rise time, see [33]. Figure 4.6 shows the comparison of a noise curve measured and evaluated with the DANTE DPP and three noise curves evaluated with a manual trapezoidal filter with different gap times.

The gap time of the trapezoidal filter in the DANTE DPP is set to  $0.224 \mu\text{s}$ . For the

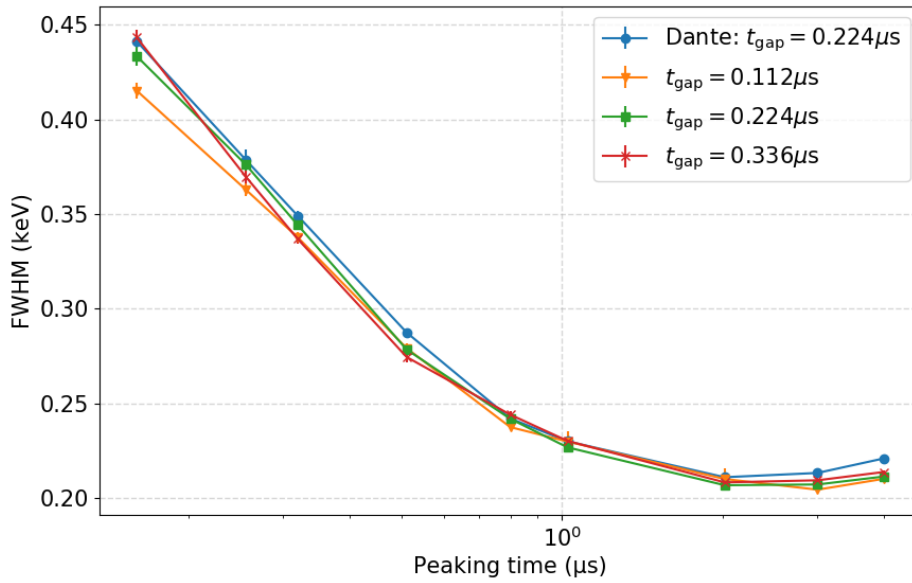


Figure 4.6: Comparison between different trapezoidal filter gap times. The blue line represents the analysis of a DANTE sweep with a gap time of  $\tau_{\text{gap}} = 0.224 \mu\text{s}$ . The orange, green and red lines correspond to the analysis of list wave data with a manual trapezoidal filter with gap times of  $\tau_{\text{gap}} = 0.112 \mu\text{s}$ ,  $\tau_{\text{gap}} = 0.224 \mu\text{s}$  and  $\tau_{\text{gap}} = 0.336 \mu\text{s}$  respectively. No significant influence of the gap time on the energy resolution is found within uncertainties.

manual trapezoidal filter gap times of 0.112  $\mu\text{s}$ , 0.224  $\mu\text{s}$  and 0.336  $\mu\text{s}$  are used. The measurement was evaluated for each of the three gap times. To obtain the energy resolution, the Mn- $K_\alpha$ -peak was fitted with a simple Gaussian function. Especially at the region of interest at a peaking time of 1  $\mu\text{s}$ , all four noise curves are in agreement within uncertainties. It can therefore be assumed that the gap time of a trapezoidal filter does not have a significant influence on the energy resolution.

## 4.5 Analysis of the influence of the peaking time on the peak position

In addition to plotting the detector resolution against the peaking time it is also useful to look at the variation of the peak position as a function of the peaking time in order to try to understand the detector response.

For this analysis, the S0-7-1 detector was used and list wave mode data was taken. In order to account for the undesired influence of the leakage current, the absolute peak position is determined, which is defined as the difference between the peak position of the Mn- $K_\alpha$  peak and the noise peak. The leakage current results in the slope of the ramps of the waveform. If ignored, it would lead to a linear increase of the peak position over peaking time.

The measurements usually do not provide a noise peak high enough to fit properly. For this reason, a noise peak is inserted manually in the measured spectra, using a trapezoidal filter and adding a trigger at the end of the recorded wave snippets, where no events are located. The peak positions of the noise peak and the Mn- $K_\alpha$  peak is then determined with a simple Gaussian fit.

Figure 4.7 shows the result for each of the seven pixels of the detector. Slave 1 to 6 show the same behaviour, the peak position decreases with increasing peaking time. At short peaking times this decrease is steeper, which can be explained by the higher noise associated with short peaking times. This leads to a worse resolution, as shown in the section 4.1, resulting in a spectrum where the Mn- $K_\alpha$  peak and the Mn- $K_\beta$  peak are no longer clearly separated but partially overlapping. Still the Mn- $K_\alpha$  peak is treated as one Gaussian peak in the fit, allowing the Mn- $K_\beta$  peak to influence the result and thus shifting the peak position to higher values of ADC. In the region of interest for this measurement, the resolution improves with higher peaking times therefore the influence of the Mn- $K_\beta$ -peak on the peak position of the Mn- $K_\alpha$  peak decreases. Hence, the behaviour of Slave 1 to 6 is expected.

However, the Master pixel follows another trend: a shift to higher peak positions at increasing peaking time. This has no physical explanation and requires further investigation.

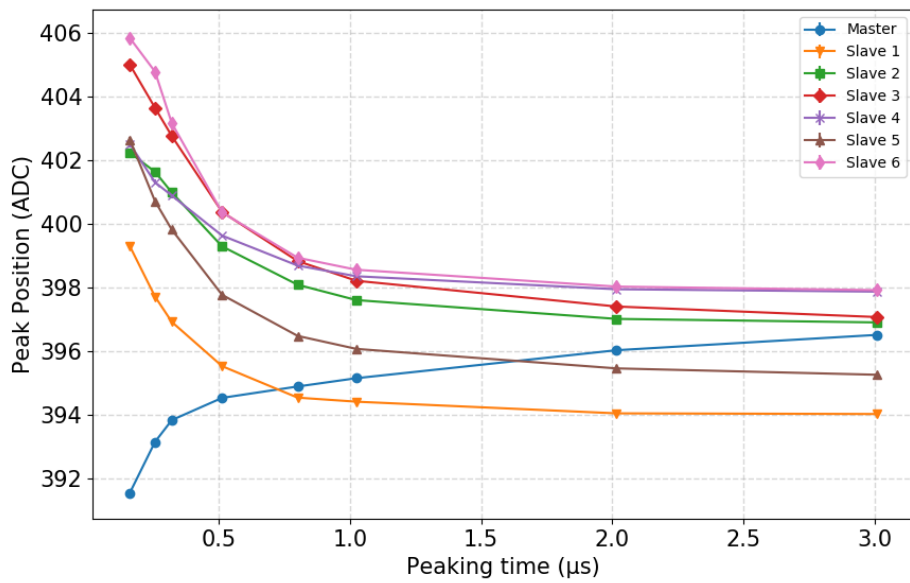


Figure 4.7: Influence of the peaking time of the trapezoidal filter on the peak position of the  $\text{Mn-}K_{\alpha}$  peak. Slave 1 to 6 show a shift to lower ADC values at increasing peaking times while the peaks of the Master shift to higher ADC values. The latter is not explained yet.



# Chapter 5

## Conclusion

To search for sterile neutrinos with a mass in the range of keV, the TRISTAN project plans to upgrade the KATRIN setup after the ongoing investigation of the effective electron anti-neutrino mass is completed. To account for the high count rates arising from a broader analysis range of the spectrum, a new detector and read-out system are developed. For that, silicon drift detectors with an integrated JFET are used. Among a high linearity and an excellent resolution, a good understanding of the noise behaviour of the detector is crucial to achieve the goals of the TRISTAN project. In this work, the main focus was the investigation of the noise behaviour of the current TRISTAN prototype generation.

The prototype detectors were investigated using an  $^{55}\text{Fe}$  source. The first part of the thesis deals with the analysis of the noise densities of two detectors in the frequency domain. Except for one pixel, the seven pixels of the detector were found to be homogeneous. A model describing the noise density based on the noise sources in a charge sensitive amplifier was compared to the measurements. With this model, the value for the capacitance is determined to be  $C = (303 \pm 6)$  fF, which is higher than the real value. This indicates a missing noise component in the model for the new generation. A comparison with a detector prototype of the previous generation confirmed that the noise density of the new generation is elevated by a factor 5 in the range of  $2 \cdot 10^5 - 1 \cdot 10^7$  Hz compared to the previous prototype.

As a second part of this thesis, the impact of the enlarged noise density on the energy resolution was studied in the time domain. At  $23^\circ\text{C}$ , the best measured energy resolution for most pixel was determined to be  $\Delta E_{\text{FWHM}} \approx 210$  eV. This value is significantly higher than the energy resolution of the previous generation,  $\Delta E_{\text{FWHM}} \approx 164$  eV, confirming the increased noise observed in the frequency domain. The cause of the additional noise requires further investigation.

The analyses in the frequency domain and in the time domain were compared, resulting in extracted values of the same order of magnitude. Both methods are therefore suitable to estimate the relevant detector information. However, the values do not match within uncertainties. The deviation amounts to 13.6 % for the leakage current, 15.8 % for the capacitance and 41.3 % for the  $\frac{1}{f}$ -coefficient.

An extension of the noise model could improve the conformity of the analysis in the frequency domain and in the time domain. It would allow for a more precise analysis of the noise spectral density, including a characterisation of the missing noise component of the new detector generation. Future investigations will include the search for the origin of the missing noise component.

This work provides a baseline for all future measurements with the current prototype generation and will serve as a basis for future noise investigations. It is the first detailed characterisation of the noise performance of the new detector generation, which is crucial for the commissioning of future, more sophisticated detector modules with more than 7 pixels.

## Bibliography

- [1] M. Goldhaber, L. Grodzins and A. W. Sunyar. »Helicity of Neutrinos«. In: *Phys. Rev.* 109.3 (1958). DOI: 10.1103/PhysRev.109.1015.
- [2] S. N. Gninenko, D. S. Gorbunov and M. E. Shaposhnikov. »Search for GeV-scale sterile neutrinos responsible for active neutrino oscillations and baryon asymmetry of the Universe«. In: *arXiv e-prints* (Jan. 2013). arXiv: 1301.5516 [hep-ph].
- [3] N. Tolich. »Final results from SNO«. In: *Journal of Physics: Conference Series* 375 (July 2012). DOI: 10.1088/1742-6596/375/1/042049.
- [4] C. Giganti, S. Lavignac, and M. Zito. »Neutrino oscillations: the rise of the PMNS paradigm«. In: *Progress in Particle and Nuclear Physics* 98 (2017), pp. 1–54. DOI: 10.1016/j.ppnp.2017.10.001.
- [5] S. Dodelson and L. M. Widrow. »Sterile neutrinos as dark matter«. In: *Phys. Rev. Lett.* 72 (1 Jan. 1994), pp. 17–20. DOI: 10.1103/PhysRevLett.72.17.
- [6] M. Aker et al. »Improved Upper Limit on the Neutrino Mass from a Direct Kinematic Method by KATRIN«. In: *Phys. Rev. Lett.* 123 (22 Nov. 2019), p. 221802. DOI: 10.1103/PhysRevLett.123.221802.
- [7] A. Loureiro et al. »Upper Bound of Neutrino Masses from Combined Cosmological Observations and Particle Physics Experiments«. In: *Phys. Rev. Lett.* 123 (8 Aug. 2019), p. 081301. DOI: 10.1103/PhysRevLett.123.081301.
- [8] E. Kh. Akhmedov, G. C. Branco and M. N. Rebelo. »Seesaw mechanism and structure of neutrino mass matrix«. In: *Physics Letters B* 478.1 (2000), pp. 215–223. ISSN: 0370-2693. DOI: 10.1016/S0370-2693(00)00282-3.
- [9] J. Angrik et al. (KATRIN Collaboration). »KATRIN Design Report 2004«. In: (2004). DOI: 10.5445/IR/270060419.
- [10] T. Brunst. »First generation prototype detectors for the TRISTAN project«. Doctor’s Thesis. Technical University of Munich, 2020. URL: <http://mediatum.ub.tum.de/?id=1540377>.
- [11] K. Urban. »Application of a TRISTAN Silicon Drift Detector as Forward Beam Monitor in KATRIN«. Master’s Thesis. Technical University of Munich, 2019.
- [12] Health Physics Society. *Tritium Fact Sheet*. URL: [https://hps.org/documents/tritium\\_fact\\_sheet.pdf](https://hps.org/documents/tritium_fact_sheet.pdf). (accessed: 12.09.2020).

- [13] J. F. Amsbaugh et al. »Focal-plane detector system for the KATRIN experiment«. In: *Nuclear Instruments and Methods in Physics Research A* 778 (Apr. 2015), pp. 40–60. DOI: 10.1016/j.nima.2014.12.116.
- [14] S. Mertens et al. »Sensitivity of next-generation tritium beta-decay experiments for keV-scale sterile neutrinos«. In: *Journal of Cosmology and Astroparticle Physics* 2015.02 (Feb. 2015), pp. 020–020. DOI: 10.1088/1475-7516/2015/02/020.
- [15] S. Mertens et al. »A novel detector system for KATRIN to search for keV-scale sterile neutrinos«. In: *Journal of Physics G: Nuclear and Particle Physics* 46.6 (May 2019), p. 065203. DOI: 10.1088/1361-6471/ab12fe.
- [16] M. Mazziotta. »Electron–hole pair creation energy and Fano factor temperature dependence in silicon«. In: *Nuclear Instruments and Methods in Physics Research Section A-accelerators Spectrometers Detectors and Associated Equipment* 584 (Jan. 2008), pp. 436–439. DOI: 10.1016/j.nima.2007.10.043.
- [17] Thermo Fisher Scientific - Materials Structural Analysis. *An Introduction to Silicon Drift Detectors*. URL: <https://www.azom.com/article.aspx?ArticleID=11973>. (accessed: 08.09.2020).
- [18] P. Lechner et al. »Silicon drift detectors for high count rate X-ray spectroscopy at room temperature«. In: *Nuclear Instruments and Methods in Physics Research Section A: Accelerators, Spectrometers, Detectors and Associated Equipment* 458 (Feb. 2001), pp. 281–287. DOI: 10.1016/S0168-9002(00)00872-X.
- [19] M. Descher. »High rate systematic effects for keV sterile neutrino searches at KATRIN«. Master’s Thesis. Technical University of Munich, 2019.
- [20] L. Bombelli et al. »“CUBE”, A low-noise CMOS preamplifier as alternative to JFET front-end for high-count rate spectroscopy«. In: *2011 IEEE Nuclear Science Symposium Conference Record*. 2011, pp. 1972–1975. DOI: 10.1109/NSSMIC.2011.6154396.
- [21] X. Pawlowski. »Characterization of the TRISTAN Silicon Drift Detectors with Krypton Conversion Electrons«. Bachelor’s Thesis. Technical University of Munich, 2018.
- [22] Laboratoire National Henri Becquerel. *Table de Radionucléides*. 2006. URL: [http://www.nucleide.org/DDEP\\_WG/Nuclides/Fe-55\\_tables.pdf](http://www.nucleide.org/DDEP_WG/Nuclides/Fe-55_tables.pdf). (accessed: 08.09.2020).
- [23] T. Eggert. »Die spektrale Antwort von Silizium-Röntgendetektoren«. Doctor’s Thesis. Technical University of Munich, 2004. URL: <https://nbn-resolving.org/urn/resolver.pl?urn:nbn:de:bvb:91-diss2004101114551>.
- [24] H. Spieler. *Semiconductor Detector Systems*. Semiconductor Science and Technology. Clarendon Press Oxford, 2005. ISBN: 9780198527848.

- [25] R. Müller. *Halbleiter-Elektronik: Rauschen*. Halbleiter-Elektronik. Springer-Verlag Berlin Heidelberg GmbH, 1979. ISBN: 9783642615016.
- [26] V. Radeka. »Low-Noise Techniques in Detectors«. In: *Annual Review of Nuclear and Particle Science* 38.1 (1988), pp. 217–277. DOI: 10.1146/annurev.ns.38.120188.001245.
- [27] C. Grupen and B. Shwartz. *Particle Detectors*. Cambridge University Press, 2008. ISBN: 9780511388668.
- [28] E. Pinotti et al. »The pn-CCD on-chip electronics«. In: *Nuclear Instruments and Methods in Physics Research Section A: Accelerators, Spectrometers, Detectors and Associated Equipment* 326.1 (1993), pp. 85–91. ISSN: 0168-9002. DOI: 10.1016/0168-9002(93)90337-H.
- [29] Internal Report presented by Peter Lechner. Halbleiterlabor der Max-Planck-Gesellschaft in München.
- [30] Private Conversation Korbinian Urban.
- [31] D. Spreng. »Energy Calibration of the TRISTAN Silicon Drift Detectors«. Bachelor's Thesis. Technical University of Munich, 2020.
- [32] V. T. Jordanov and G. F. Knoll. »Digital synthesis of pulse shapes in real time for high resolution radiation spectroscopy«. In: *Nuclear Instruments and Methods in Physics Research Section A: Accelerators, Spectrometers, Detectors and Associated Equipment* 345.2 (1994), pp. 337–345. ISSN: 0168-9002. DOI: 10.1016/0168-9002(94)91011-1.
- [33] C. Forstner. »Pulse Shape Analysis with the TRISTAN Silicon Drift Detector«. Bachelor's Thesis. Technical University of Munich, 2020.

## Acknowledgements

I would like to thank everyone who supported me during my bachelor thesis, especially:

- **Prof. Dr. Susanne Mertens:** Thank you for giving me the opportunity to do my bachelor's thesis in your group and for your support during my work.
- **Tim Brunst:** Thank you for the supervision during my bachelor's thesis, for all the questions you have patiently answered and for all the tips and constructive criticism you have given me while reading my thesis.
- **Korbinian Urban:** Thank you for the endurance to answer all my questions around noise theory, noise density and simulations.
- **Daniel Siegmann:** Thank you for your tips as well as all the kind words and encouragement.
- **Container ground floor:** Thank you all for the kind conversations and a pleasant work environment.
- **Daniela Spreng:** Thank you for your moral support and for always having time for me when I got stuck.